



## Available online at www.sciencedirect.com

# **ScienceDirect**

Comput. Methods Appl. Mech. Engrg. 416 (2023) 116332

Computer methods in applied mechanics and engineering

www.elsevier.com/locate/cma

# Phase-field modeling of stochastic fracture in heterogeneous quasi-brittle solids

Jian-Ying Wu<sup>a,b,\*</sup>, Jing-Ru Yao<sup>a</sup>, Jia-Liang Le<sup>c</sup>

<sup>a</sup> Department of Civil Engineering, South China University of Technology, 510641 Guangzhou, China
<sup>b</sup> State Key Laboratory of Subtropical Building and Urban Science, South China University of Technology, 510641 Guangzhou, China
<sup>c</sup> Department of Civil, Environmental and Geo- Engineering, University of Minnesota, Minneapolis, MN 55455, United States of America

Received 15 May 2023; received in revised form 26 July 2023; accepted 27 July 2023 Available online xxxx

#### Abstract

Owing to the random nature of heterogeneity, damage and fracture behavior of quasi-brittle materials exhibits a considerable degree of uncertainty. Computational modeling of stochastic fracture in quasi-brittle materials has become an indispensable tool for analysis and design of engineering structures. To this end, we present in this paper a computational framework to capture probabilistic fracture in heterogeneous quasi-brittle solids by combining the random field theory and the phase-field cohesive zone model (PF-CZM). The spatial variation of the material strength and fracture energy is represented by a cross-correlated bivariate random field generated by the Karhunen-Loève expansion. The recently proposed PF-CZM is employed to simulate the stochastic crack nucleation and propagation in quasi-brittle solids. The objectivity of the Monte-Carlo simulation is achieved by imposing a specific condition on the phase-field length scale parameter and the correlation length of the random field. In particular, upon this condition the width of the fracture process zone (FPZ) is considerably smaller than the correlation length of the random field such that the material inside the FPZ does not exhibit significant spatial variations of mechanical properties. As the fracture energy is intrinsically incorporated in the PF-CZM, it is unnecessary in this case to explicitly consider the FPZ width. The resulting probabilistic PF-CZM together is applied to the Monte-Carlo simulations of fracture in concrete structures of different geometries. It is shown that the stochastic simulation results are insensitive to both the phase-field length scale parameter and the finite element mesh discretization as in the previous deterministic analyses. Enhanced with the specific condition on the involved characteristic lengths, the PF-CZM provides a viable tool for stochastic simulations of damage and fracture in quasi-brittle structures.

© 2023 Elsevier B.V. All rights reserved.

Keywords: Probabilistic phase-field model; Random field representation; Monte-Carlo simulation; Stochastic fracture; Heterogeneous solids; Mesh objectivity

#### 1. Introduction

Quasi-brittle materials are often composed of brittle matrix and randomly distributed inhomogeneities. Typical examples include concrete, tough ceramics, rocks, and particulate composites. The random nature of the material microstructure inevitably causes a considerable degree of uncertainty in the macroscopic mechanical behavior,

<sup>\*</sup> Corresponding author at: Department of Civil Engineering, South China University of Technology, 510641 Guangzhou, China. E-mail address: jywu@scut.edu.cn (J.-Y. Wu).

such as the ultimate load capacity and the fracture pattern. These uncertainties have important implications for the reliability and safety of built structures. Therefore, it is of great significance to develop robust computational methods in prediction of the stochastic fracture behavior for reliability-based analysis and design of quasi-brittle structures.

The stochastic finite element method (SFEM) provides a versatile tool for probabilistic analysis of structural behavior. The SFEM requires a realistic representation of the spatial variation of the random material properties. If we consider that the size of finite element is sufficiently large compared to the correlation lengths of the random material properties, we can treat the random material properties of each finite element as a set of independent and discrete random variables, which are sampled directly from the corresponding cumulative distribution functions (CDFs). In a general setting, a more versatile approach is to represent the spatial variation of the mechanical properties by random fields [1], which are characterized by the CDFs of material properties and the covariance and cross-covariance functions. With the advances of experimental techniques, such as X-ray computed tomography (XCT) [2,3], destructive testing [4,5], non-destructive testing [6,7], etc., for replicating the micro-structure and identifying the statistical information of mechanical parameters, the random field representation of material properties has been increasingly used for heterogeneous solids [8–10].

Stochastic fracture in quasi-brittle solids often involves crack nucleation at random locations and propagation along arbitrary directions. The specimen could also exhibit different prevailing failure patterns. In the literature, both the continuous and discontinuous approaches to deterministic fracture [11] have been applied to modeling the stochastic fracture process in heterogeneous materials. For instance, the cohesive crack model has been extended to stochastic analysis of concrete structures [12,13]. Though the cohesive crack model provides a straightforward means for modeling the fracture behavior, it lumps the fracture process zone (FPZ) into a line, ignoring the effect of multiaxial stress state on the fracture process even for a single dominant fracture mode [14]. Meanwhile, the cohesive crack model also suffers from the notorious mesh bias, to overcome which one would need a robust algorithm to track the crack path. Carmeliet and Hens [15] proposed a probabilistic nonlocal damage model with a bivariate random field to simulate the stochastic behavior of strain-softening materials. Castillo et al. [16] recently applied the nonlocal damage model to fracture of concrete materials, with Young's modulus and the failure strength being treated as two independent random fields. However, one fundamental and unsolved issue of nonlocal damage model is the treatment of nonlocal interaction at the structural boundaries [17–19]. This issue has important implications for modeling the crack propagation, during which new boundaries are created.

An important issue in computational modeling of quasi-brittle fracture is the spurious mesh sensitivity arising from the localization instability. This issue has been investigated extensively for deterministic simulations. A class of methods, called the localization limiters, which include the crack band model and nonlocal models, were developed to mitigate the issue of mesh dependence. Recent studies have shown that, in stochastic simulations, the mesh sensitivity is not only related to energy regularization but also is affected by the sampling of the random constitutive properties [20,21]. A mechanism-based sampling method was recently proposed in the context of continuum damage constitutive model [21]. The method was formulated for the case where the mesh size is chosen to be larger than the FPZ width and the correlation lengths of the random constitutive properties, a typical scenario for the analysis of large-scale structures.

Over the past decade, the variational phase-field approach has attracted significant attention for computational modeling of fracture in solids [22–24]. It is able to deal with those complex fracture processes, e.g., crack nucleation, propagation, and branching, in a standalone variational framework without relying on any crack tracking schemes. The earlier development of the phase-field models, e.g. AT1 [25,26] and AT2 [23,27], focused on brittle fracture. These models have recently been extended to simulations of stochastic fracture in heterogeneous solids; see [28–32] among others. However, the AT1 and AT2 models rely on the fracture energy only. In order to capture the material's failure strength, one needs to consider the phase-field length scale as a material property which could be large for quasi-brittle materials (e.g. 300 mm for concrete). Consequently, the energy dissipation would be severely over-estimated.

In a series of recent studies [33–35], the phase-field cohesive zone model (PF-CZM) was proposed for brittle and quasi-brittle fracture. Compared to the aforementioned AT1/AT2 models, in the PF-CZM the material strength is introduced directly as a material property and the phase-field length scale is treated as a numerical parameter that can be chosen to be arbitrarily small or a physical parameter so long as it is small enough. In this way, the model takes into account both strength and fracture parameters, which is able to capture both strength and fracture

energy governed failure mechanisms. It has been shown that the PF-CZM is insensitive to the phase-field length scale and independent of the mesh discretization [33,35,36]. Furthermore, the model is able to reproduce different types of strain-softening behavior for quasi-brittle materials, such as linear softening, exponential softening, and hyperbolic softening [37] and so on. The model has recently been combined with the XCT imaging technique [38] for modeling fracture of heterogeneous continua. Subsequently, Huang et al. [39] constructed the random field for the mechanical properties based on the XCT image, nevertheless, with the cross-correlation between material parameters ignored. Hai and Li [40] applied the PF-CZM to stochastic fracture in concrete assuming full correlation between the failure strength and the fracture energy.

The recent study by Le and co-workers [20,21] showed that the sampling method of the random constitutive properties in the finite element has profound implications for the objectivity of stochastic finite element (FE) simulations. In the random field representation of constitutive properties the essential length parameter is the correlation length. Another length parameter in FE analysis is the mesh size. Regarding the crack band method [20,21,41] have investigated the interaction between these different length scales for stochastic simulations and the consequences for the results of the stochastic FE simulations. It was found that inappropriate choices of these length parameters could lead to spurious mesh dependence in the simulations and special cares are needed to guarantee the numerical objectivity. The same conclusion also holds for other deterministic models with strain softening. In particular, those deterministic nonlocal approaches, e.g., the phase-field fracture models like the PF-CZM with an extra intrinsic length scale parameter, cannot be directly applied to stochastic fracture simulations unless some conditions are fulfilled. Recently, in [42] it was suggested that the phase-field length scale parameter be much smaller than the correlation length of the random field such that the predicted probabilistic characteristics are not affected by the former. However, so far no specific conditions between these two length parameters, to the best knowledge of the authors, have been addressed before.

In this study, we present a computational framework to capture probabilistic fracture in heterogeneous quasi-brittle solids by combining the random field theory and the PF-CZM. The framework uses the Karhunen-Loève (K-L) expansion method to generate a cross-correlated bivariate random field of the material strength and the fracture energy. For each sample of the spatial random material strength and fracture energy, the PF-CZM is used to simulate the fracture behavior of the structure. A specific condition on the phase-field length scale parameter and the correlation length of the random field is, for the first time, proposed to guarantee objectivity of the stochastic FE simulations. Upon this condition the material inside the FPZ does not exhibit significant spatial variations of mechanical properties such that it is unnecessary to explicitly consider the FPZ width in the resulting probabilistic PF-CZM. Note that only tension-dominated fracture in heterogeneous solids is considered in this work in order to avoid the complexity in modeling the spatial variation of extra mechanical properties. Moreover, though 3D probabilistic analysis might be more realistic, only 1D and 2D problems are considered here for the sake of simplicity. However, as both the K-L expansion method and the probabilistic PF-CZM are not dimension limited, extension of the present study to 3D problems are straightforward so long as the computational cost brought by Monte-Carlo simulations is acceptable.

The paper is organized as follows. Section 2 presents the phase-field cohesive modeling of stochastic fracture in heterogeneous solids by combining the PF-CZM with the random field theory. Section 3 discusses the numerical implementation of the PF-CZM in context of the stochastic finite element method. Section 4 is devoted to validation of the resulting probabilistic PF-CZM. The effect of various length parameters (the correlation length, the phase-field length scale parameter, the mesh size of the FE and the grid size of the random field, etc..) on the stochastic fracture characteristics, e.g., crack patterns, failure modes and global responses, etc., are studied. In Section 5 the probabilistic PF-CZM is applied to the modeling of stochastic fracture in several representative numerical examples.

## 2. Computational framework to capture probabilistic fracture

The computational framework is anchored by the theory of random field [1] and the phase-field cohesive zone model (PF-CZM). As shown in Fig. 1(a), let  $\Omega \subset \mathbb{R}^{n_{\text{dim}}}$  be the reference configuration of a cracking solid, with the external boundary denoted by  $\partial \Omega \subset \mathbb{R}^{n_{\text{dim}}-1}$  and the outward normal vector by  $\boldsymbol{n}$ . The body forces (per unit volume)  $\boldsymbol{b}$  are distributed within the whole domain  $\Omega$  and the prescribed tractions  $\boldsymbol{t}^*$  are applied to the part of boundary  $\partial \Omega_t \subset \partial \Omega$ . The resulting deformation of the solid is described by the displacement field  $\boldsymbol{u}(\boldsymbol{x})$  and the (infinitesimal) strain field  $\boldsymbol{\epsilon}(\boldsymbol{x}) := \nabla^{\text{sym}} \boldsymbol{u}(\boldsymbol{x})$ , for the symmetric gradient operator  $\nabla^{\text{sym}}(\cdot)$  with respect to the spatial coordinate  $\boldsymbol{x}$ . For the well-posedness of the boundary value problem, given displacements  $\boldsymbol{u}^*$  are imposed on the complementary boundary  $\partial \Omega_u = \partial \Omega \setminus \partial \Omega_t$ . All the sharp cracks in the solid are collected in the set  $\mathcal{S} \subset \mathbb{R}^{n_{\text{dim}}-1}$ , with the normal vector of the crack surfaces signified by  $\boldsymbol{n}_{\mathcal{S}}$ .

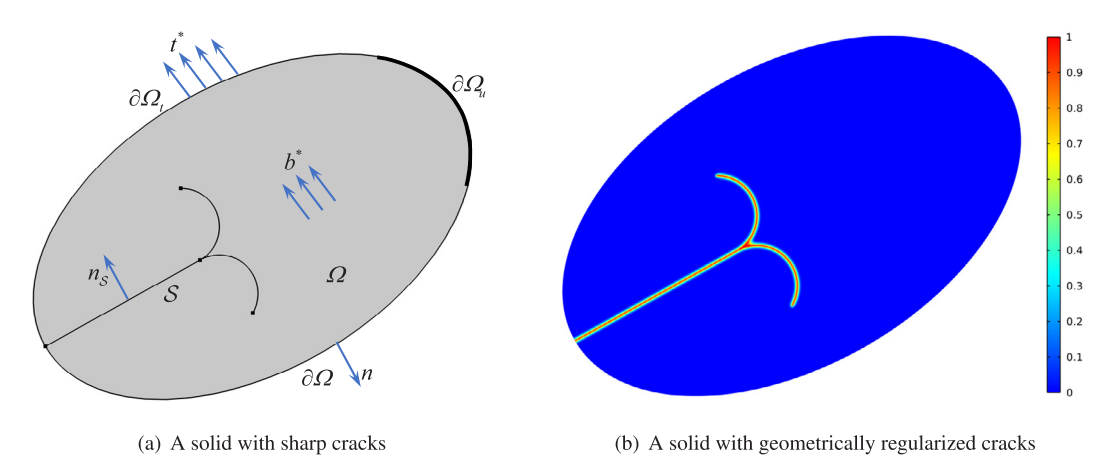


Fig. 1. A cracking solid with sharp cracks and the geometric regularization.

## 2.1. Phase-field cohesive zone model

In this study, the fracture behavior is simulated by the PF-CZM recently developed by Wu [33], Wu [34] and Wu and Nguyen [35]. As shown in Fig. 1(b), in phase-field models for fracture [24,43], the sharp crack S is regularized over a localization band  $\mathcal{B} \subseteq \Omega$ , in which the crack phase-field or damage field  $d(x) : \mathcal{B} \to [0, 1]$  localizes. The damage field satisfies the irreversibility condition  $\dot{d}(x) \ge 0$ , where  $\dot{x}$  denotes the time derivative of quantity x.

In the phase-field model, a length parameter b is introduced to measure the width of the damage band. When it vanishes  $(b \to 0)$ , a sharp crack is recovered. The external boundary of the localization band  $\mathcal{B}$  is denoted by  $\partial \mathcal{B}$ and the outward unit normal vector by  $n_R$ . Note that the localization band is neither prescribed a priori nor fixed all along, but rather, it is automatically updated during the crack propagation. Proper Dirichlet boundary conditions, e.g., d(x) = 1 for pre-existing cracks, can be imposed as well.

For solids under pure mechanical loading, the phase-field model is described by the following set of equations

$$\begin{cases} \nabla \cdot \boldsymbol{\sigma} + \boldsymbol{b} = \boldsymbol{0} & \text{in } \Omega \\ \boldsymbol{\sigma} \cdot \boldsymbol{n} = \boldsymbol{t}^* & \text{on } \partial \Omega_t \end{cases}$$
 (2.1a)

$$\begin{cases} \nabla \cdot \boldsymbol{\sigma} + \boldsymbol{b} = \boldsymbol{0} & \text{in } \Omega \\ \boldsymbol{\sigma} \cdot \boldsymbol{n} = \boldsymbol{t}^* & \text{on } \partial \Omega_t \end{cases}$$

$$\begin{cases} \nabla \cdot \boldsymbol{q} + Q \le 0 & \text{in } \mathcal{B} \\ \boldsymbol{q} \cdot \boldsymbol{n}_{\mathcal{B}} \ge 0 & \text{on } \partial \mathcal{B} \end{cases}$$

$$(2.1a)$$

for the crack phase-field flux vector  $\boldsymbol{q}$  and the source term  $\boldsymbol{Q}$ 

$$q = \frac{2b}{c_{\alpha}}G_{\rm f} \nabla d, \qquad Q = -\bar{Y}\frac{\mathrm{d}\omega(d)}{\mathrm{d}d} - \frac{G_{\rm f}}{c_{\alpha}b}\frac{\mathrm{d}\alpha(d)}{\mathrm{d}d}$$
 (2.1c)

where  $G_f$  = fracture energy,  $\bar{Y}$  = crack driving force,  $\alpha(d)$  = geometric crack function,  $\omega(d)$  = damage function, and  $c_{\alpha} = 4 \int_{0}^{1} \sqrt{\alpha(d)} \, dd$ .

Though more complicated damage models can be adopted (see [44]), the following isotropic one is usually sufficient

$$\sigma = \omega(d)\bar{\sigma}, \qquad \bar{Y} = \frac{1}{2E_0} \langle \bar{\sigma}_1 \rangle^2$$
 (2.2)

where  $\bar{\sigma} = \mathbb{E}_0$ :  $\epsilon$  is the effective stress tensor, with  $\mathbb{E}_0$  being the fourth-order elasticity tensor;  $E_0$  is Young's modulus of the material, respectively;  $\bar{\sigma}_1$  denotes the major principle value of the effective stress  $\bar{\sigma}$ ; Macaulay brackets  $\langle \cdot \rangle$  are defined as  $\langle x \rangle = \max(x, 0)$ .

The damage function  $\omega(d)$  describes the stiffness degradation, which has to be monotonically decreasing with damage variable d. By contrast, function  $\alpha(d)$ , which characterizes homogeneous evolution of the crack phasefield, is a monotonically increasing function with d. Based on the previous studies [33–35], we adopt the following

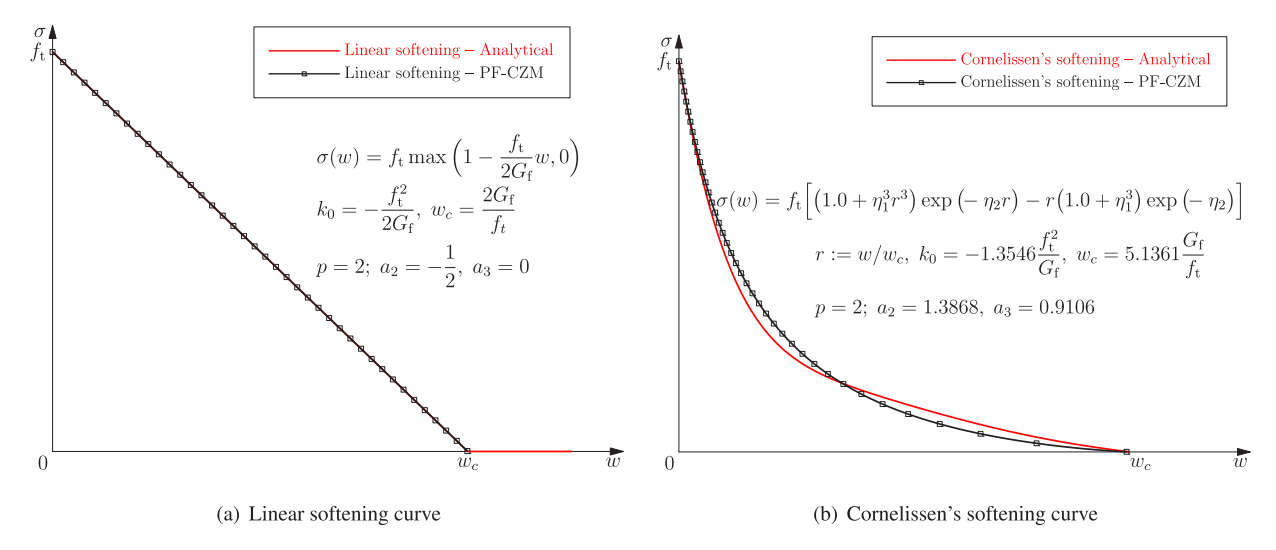


Fig. 2. Typical softening curves and the phase-field approximations.

expression for  $\alpha(d)$  and  $\omega(d)$ :

$$\begin{cases} \alpha(d) = 2d - d^2 \\ \omega(d) = \frac{(1-d)^p}{(1-d)^p + a_1 d \cdot P(d)} \end{cases} \qquad P(d) = 1 + a_2 d + a_3 d^2 + \cdots$$
 (2.3)

for the parameters  $p \ge 2$ , and  $a_1$ ,  $a_2$  and  $a_3$ 

$$a_1 = \frac{4}{\pi} \cdot \frac{\ell_{\text{ch}}}{b}, \qquad a_2 = 2\beta_k^{2/3} - \left(p + \frac{1}{2}\right), \qquad a_3 = \begin{cases} 0 & p > 2\\ \frac{1}{2}\beta_w^2 - \left(1 + a_2\right) & p = 2 \end{cases}$$
 (2.4)

where the Irwin internal length  $\ell_{\rm ch} := E_0 G_{\rm f}/f_{\rm t}^2$  is related to the length of the FPZ, with  $f_{\rm t}$  being the failure strength of the material; the ratios  $\beta_k$  and  $\beta_w$  compare the initial slope  $k_0 < 0$  and the ultimate crack opening  $w_c$  of the traction – separation law against those of the linear softening curve, i.e.,

$$\beta_k := \frac{k_0}{-\frac{1}{2}f_t^2/G_f} \ge 1, \qquad \beta_w := \frac{w_c}{2G_f/f_t}$$
(2.5)

For instance, the linear softening law for brittle fracture and the Cornelissen et al. [37] softening curve for concrete can be reproduced or approximated as shown in Fig. 2 with the following parameters (see Remark 2.1)

Linear softening curve: 
$$p=2, a_2=-\frac{1}{2}, a_3=0$$
 Cornelissen's softening curve:  $p=2, a_2=1.3868, a_3=0.9106$  (2.6)

For fracture in homogeneous solids, it is exactly the incorporation of the parameter  $a_1 \propto \ell_{\rm ch}/b$  in the degradation function  $\omega(d)$  that ensures the predicted crack patterns, failure modes and global responses to be insensitive to the phase-field length scale parameter b, as long as the latter is small enough; see Remark 2.2.

**Remark 2.1.** At the first glace, Fig. 2(b) exhibits some "apparent discrepancy" between the Cornelissen et al. [37] softening curve and the PF-CZM approximation with the parameters in Eq.  $(2.6)_2$ . However, this so-called "apparent discrepancy" does not present real issues since: (i) the Cornelissen softening curve is neither a universal law nor a unique expression, but is just a fitting curve of experimental data applicable for normal concrete; (ii) generally it is not the specific expression of a softening curve, but the associated characteristics, i.e., the failure strength  $f_t$ , the fracture energy  $G_f$ , the initial slope  $k_0$  and the ultimate crack opening  $w_c$ , that determine the fracture pattern and failure behavior of brittle and quasi-brittle solids; see Bažant and Planas (1997); (iii) it is not difficult for the above PF-CZM to approximate the Cornelissen softening curve with better precision by using a higher-order polynomial

P(d) in Eq.  $(2.3)_2$ ; see Appendix. Note that in [45], upon a particular relationship between the degradation function  $\omega(d)$  and the geometric one  $\alpha(d)$ , an integral transform was proposed to determine explicitly the characteristic functions for a given softening curve. However, this scheme does not necessarily guarantee the irreversibility of crack evolution (spurious thinning of the crack band) for general softening curves.  $\square$ 

**Remark 2.2.** In order to guarantee the capability of phase-field models in reproducing the energy dissipation during fracture, the length scale parameter b had better be as small as possible. Practically, this requisite is fulfilled with the following condition [34,46]

$$b \le \min\left(\frac{8}{3\pi}\ell_{\rm ch}, \frac{1}{100}L \sim \frac{1}{50}L\right)$$
 (2.7)

for the characteristic size L of the structure. Upon the above condition, the analytical result and extensive numerical studies have verified that the above PF-CZM is insensitive to the phase-field length scale for brittle and cohesive fracture [33–35]. In this work we will demonstrate that this length scale insensitivity also holds for stochastic fracture in heterogeneous solids upon an extra condition.  $\Box$ 

## 2.2. Cross-correlated bivariate random field for the mechanical fracture properties

Modeling tensile fracture of quasi-brittle materials requires both the material's tensile strength and mode I fracture energy. The material strength determines whether and where crack nucleation occurs, and the fracture energy governs the crack propagation. Therefore, stochastic simulations of quasi-brittle fracture should at minimum account for the spatial randomness of these two mechanical properties [20,21,47]. The spatially variation in Young's modulus is not considered in this work.

Recent studies have shown that the tensile strength of quasi-brittle materials can be described by a Gaussian–Weibull grafted distribution [19,48,49]. This distribution function was derived from the atomistic fracture mechanics and a statistical multiscale model. In this study, a bivariate stationary random field  $\{\chi(x,\theta); x \in \Omega \subseteq \mathbb{R}^{n_{\text{dim}}}\}$  of lognormal distribution is used to model the variations of the tensile strength  $f_t$  and fracture energy  $G_f$ , where  $\theta$  is a set of random variables and  $n_{\text{dim}} = 1, 2, 3$  is the geometrical dimension of the spatial domain  $\Omega$ . The reasons for choosing lognormal distributions are two-fold: (1) for the given mean and variance, the lognormal distribution gives a similar prediction of the cumulative distribution as the Gaussian–Weibull grafted distribution except for far left and right tails; nevertheless, for stochastic FE analysis, the focus is placed on the prediction of the mean and variance of the response, which in most cases are minimally affected by the tail behavior; (2) as compared to the Gaussian–Weibull grafted distribution, it is more straightforward to general random fields with lognormal distributions.

Let the bivariate random field be denoted by  $\chi(x, \theta)$ . At a given point  $x_i$ , the random field  $\chi(x_i, \theta)$  degenerates to a random variable  $\chi$ , with the cumulative distribution function (CDF) denoted by  $F_{\chi}(\chi)$ . In order to represent the non-Gaussian random field  $\chi$ , a common strategy is to generate an underlying Gaussian random field  $\tilde{\chi}$  and then transform it via the isoprobabilistic (memoryless) transformation

$$\chi(\mathbf{x}, \boldsymbol{\theta}) = F_{\mathbf{x}}^{-1} \left[ \Phi(\tilde{\chi}(\mathbf{x}, \boldsymbol{\theta})) \right]$$
 (2.8)

where  $\Phi(\cdot)$  is the CDF of the Gaussian random field  $\tilde{\chi}$ . Specifically, for the lognormal bivariate random field  $\chi$ , we introduce a random field  $\tilde{\chi} = \ln \chi$ , i.e.  $\tilde{\chi}_1 = \ln f_t$  and  $\tilde{\chi}_2 = \ln G_f$ . Both  $\tilde{\chi}_1$  and  $\tilde{\chi}_2$  follow a Gaussian distribution, with the mean and variance given by

$$\tilde{\mu}_i = \ln \mu_i - \frac{1}{2} \ln(1 + \delta_i^2), \qquad \tilde{\sigma}_i^2 = \ln(1 + \delta_i^2)$$
(2.9)

where  $\delta_i$   $(i=1,2)=\sigma_i/\mu_i$  are the coefficients of variation (CoV) of  $f_t$  and  $G_f$ , respectively;  $\mu_i,\sigma_i=$  the mean values and standard deviations of  $f_t$  and  $G_f$ .

The standardized Gaussian variable of  $\tilde{\chi}_i$  is denoted by  $\bar{\chi}_i$ , i.e.  $\bar{\chi}_i = (\tilde{\chi}_i - \tilde{\mu}_i)/\tilde{\sigma}_i$ . Clearly,  $\bar{\chi}_i$  have a zero mean and unit standard deviation. The covariance function  $C_{\bar{\chi}_i}$  of  $\bar{\chi}_i(x)$  is given by

$$C_{\bar{\mathbf{x}}_i}(\mathbf{x}_j, \mathbf{x}_k) = \sigma_{\bar{\mathbf{x}}_i}(\mathbf{x}_j) \, \sigma_{\bar{\mathbf{x}}_i}(\mathbf{x}_k) R_{\bar{\mathbf{x}}_i}(\mathbf{x}_j, \mathbf{x}_k) = R_{\bar{\mathbf{x}}_i}(\tau) \tag{2.10}$$

In the above equation, we used the fact that  $\sigma_{\bar{\chi}_i}(x) = 1$  at any given point x and the random field is homogeneous and isotropic. The auto-correlation function  $R_{\bar{\chi}}(\tau)$  defines the statistical dependence between two random variables,

with  $\tau = |x_j - x_k|$  being the distance between two spatial points  $x_j$  and  $x_k$ . In order to be differentiable at zero and separable along various dimensions, the auto-correlation function of Gaussian distribution is adopted [1]

$$R_{\bar{\chi}_i}(\tau) = \prod_{n=1}^{n_{\text{dim}}} \exp\left[-\frac{\pi}{4} \left(\frac{\tau_n}{\ell_n}\right)^2\right] = \exp\left[-\frac{\pi}{4} \left(\frac{\tau}{\ell}\right)^2\right]$$
 (2.11)

where  $\tau_n$  is the distance along the spatial direction  $1 \le n \le n_{\text{dim}}$ , and the correlation length  $\ell_n$  characterizes the spatial variation along that direction. Here an identical auto-correlation length  $\ell_n = \ell$  is considered in all spatial dimensions. Here we consider that  $\bar{\chi}_1$  and  $\bar{\chi}_2$  have the same correlation functions  $R_{\bar{\chi}}(\tau)$ . Accordingly, the cross-correlated structure can be represented by the following correlation function matrix  $C_p$ 

$$C_{R} = \begin{bmatrix} C_{\bar{\chi}_{1}} & C_{\bar{\chi}_{1}\bar{\chi}_{2}} \\ C_{\bar{\chi}_{1}\bar{\chi}_{2}} & C_{\bar{\chi}_{2}} \end{bmatrix} = \begin{bmatrix} C_{\bar{\chi}} & \bar{\rho}_{12}C_{\bar{\chi}} \\ \bar{\rho}_{12}C_{\bar{\chi}} & C_{\bar{\chi}} \end{bmatrix} = C_{\bar{\chi}}C_{\rho}$$

$$(2.12)$$

for the correlation coefficient matrix C

$$C_{\rho} = \begin{bmatrix} 1 & \bar{\rho}_{12} \\ \bar{\rho}_{12} & 1 \end{bmatrix} \tag{2.13}$$

Note that, as the transformation (2.8) distorts the correlation structure of the field  $\chi$ , the correlation coefficient  $\rho_{12}$  of the field  $\chi_1$  and  $\chi_2$  needs to be modified accordingly by, e.g., the Nataf transformation [50,51] such that  $\rho_{12} \neq \bar{\rho}_{12}$ .

In this study, the random field is generated by the Karhunen-Loève (K-L) expansion method [52–54]. In this method, the random field is expressed as a direct sum of orthogonal projections in the Hilbert space. In particular, a zero-mean, homogeneous Gaussian random field  $\bar{\chi}(x,\theta)$  can be represented by

$$\bar{\chi}(x,\theta) = \sum_{k=1}^{\infty} \sqrt{\lambda_k} \, \zeta_k(\theta) \phi_k(x) \approx \sum_{k=1}^{K} \sqrt{\lambda_k} \, \zeta_k(\theta) \phi_k(x)$$
(2.14)

where  $\zeta(\theta) = \{\zeta_k(\theta)\}$  is a set of independent standard Gaussian variables of zero mean and unit variance;  $\lambda_k$  and  $\phi_k(x)$  are the eigenvalues and the eigenfunctions of the auto-covariance function matrix  $C_{\bar{\chi}} = [C_{\bar{\chi}}]$ , given by the following homogeneous Fredholm integral equation of the second kind

$$\int C_{\bar{\chi}}(x_i, x_j) \, \phi_k(x_i) \, \mathrm{d}x_j = \lambda_k \phi_k(x_i) \tag{2.15}$$

where the eigenfunctions  $\phi_k$  form a set of orthogonal bases [54].

The truncated K-L expansion with a finite number of terms is usually adopted in practical applications [55]. It suffices to consider only K eigenmodes corresponding to the largest eigenvalues of interest, with the summation  $\sum_{k=1}^K \lambda_k$  larger than 99% of the trace of the covariance function matrix  $C_{\bar{\chi}}$  [56]. Specifically, in order to generate the discretized samples of the random fields  $\bar{\chi}_1$  and  $\bar{\chi}_2$ , we first need two sets of independent standard Gaussian variables  $\zeta_1(\theta) = \{\zeta_{1_k}(\theta)\}$  and  $\zeta_2(\theta) = \{\zeta_{2_k}(\theta)\}$ . The following three cases can be considered:

• If  $\bar{\chi}_1$  is independent of  $\bar{\chi}_2$ , i.e.,  $\bar{\rho}_{12} = 0$ , the stochastic samples can be generated separately by the truncated K-L expansion (2.14)

$$\begin{cases} \bar{\boldsymbol{\chi}}_{1} \approx \sum_{k=1}^{K} \sqrt{\lambda_{k}} \, \zeta_{1_{k}}(\boldsymbol{\theta}) \, \boldsymbol{\phi}_{k}(\boldsymbol{x}) \\ \bar{\boldsymbol{\chi}}_{2} \approx \sum_{k=1}^{K} \sqrt{\lambda_{k}} \, \zeta_{2_{k}}(\boldsymbol{\theta}) \, \boldsymbol{\phi}_{k}(\boldsymbol{x}) \end{cases}$$

$$(2.16)$$

• If  $\bar{\chi}_1$  is fully dependent on  $\bar{\chi}_2$ , i.e.,  $\bar{\rho}_{12} = 1$ , the stochastic samples of  $\bar{\chi}_1$  are first generated by the truncated K-L expansion (2.14) and then the samples of  $\bar{\chi}_2$  are given by  $\bar{\chi}_2 = c\bar{\chi}_1$ , i.e.,

$$\begin{cases} \bar{\boldsymbol{\chi}}_1 \approx \sum_{k=1}^K \sqrt{\lambda_k} \, \zeta_{1_k(\boldsymbol{\theta})} \, \boldsymbol{\phi}_k(\boldsymbol{x}) \\ \bar{\boldsymbol{\chi}}_2 = c \, \bar{\boldsymbol{\chi}}_1 \end{cases}$$
 (2.17)

where c = the proportionality coefficient between  $\bar{\chi}_1$  and  $\bar{\chi}_2$ .

• If  $\bar{\chi}_1$  and  $\bar{\chi}_2$  are cross-correlated, i.e.,  $\bar{\rho}_{12} \in (0, 1)$ , the stochastic samples of  $\bar{\chi}_1$  and  $\bar{\chi}_2$  have to be generated in pairs. We first introduce the spectral decomposition of the correlation coefficient matrix  $C_\rho$ 

$$\boldsymbol{C}_{\rho} = \begin{bmatrix} 1 & \bar{\rho}_{12} \\ \bar{\rho}_{12} & 1 \end{bmatrix} = \begin{bmatrix} \eta_{11} & \eta_{12} \\ \eta_{21} & \eta_{22} \end{bmatrix} \begin{bmatrix} \hat{\rho}_{1} & 0 \\ 0 & \hat{\rho}_{2} \end{bmatrix} \begin{bmatrix} \eta_{11} & \eta_{12} \\ \eta_{21} & \eta_{22} \end{bmatrix}^{\mathrm{T}}$$
(2.18)

where  $\{\eta_{11}, \eta_{21}\}^T$  and  $\{\eta_{12}, \eta_{22}\}^T$  represent the eigenvectors of the correlation coefficient matrix  $C_\rho$ , associated with the eigenvalues  $\hat{\rho}_1$  and  $\hat{\rho}_2$ , respectively. Accordingly, the cross-correlated Gaussian random fields  $\bar{\chi}_1$  and  $\bar{\chi}_2$  are generated in pairs as

$$\begin{bmatrix} \bar{\mathbf{\chi}}_1 \\ \bar{\mathbf{\chi}}_2 \end{bmatrix} \approx \sum_{k=1}^{2K} \sqrt{\bar{\lambda}_k} \begin{bmatrix} \zeta_{1_k}(\boldsymbol{\theta}) & 0 \\ 0 & \zeta_{2_k}(\boldsymbol{\theta}) \end{bmatrix} \bar{\boldsymbol{\phi}}_k(\boldsymbol{x})$$
 (2.19)

where the eigenvalue matrix  $\bar{\lambda} = \text{Diag}[\bar{\lambda}_k]$  and the eigenfunction matrix  $\bar{\phi}(x) = [\bar{\phi}_k(x)]$  of the correlation matrix (2.12) are expressed as [56]

$$\bar{\lambda} = \text{Diag} \Big[ \hat{\rho}_1 \lambda_1, \dots, \hat{\rho}_1 \lambda_k, \dots, \hat{\rho}_1 \lambda_K, \hat{\rho}_2 \lambda_1, \dots, \hat{\rho}_2 \lambda_k, \dots, \hat{\rho}_2 \lambda_K \Big]$$
(2.20a)

$$\bar{\boldsymbol{\phi}} = \begin{bmatrix} \eta_{11} \boldsymbol{\phi}_1 & \dots & \eta_{11} \boldsymbol{\phi}_k & \dots & \eta_{11} \boldsymbol{\phi}_K & \eta_{12} \boldsymbol{\phi}_1 & \dots & \eta_{12} \boldsymbol{\phi}_k & \dots & \eta_{12} \boldsymbol{\phi}_K \\ \eta_{21} \boldsymbol{\phi}_1 & \dots & \eta_{21} \boldsymbol{\phi}_k & \dots & \eta_{21} \boldsymbol{\phi}_K & \eta_{22} \boldsymbol{\phi}_1 & \dots & \eta_{22} \boldsymbol{\phi}_k & \dots & \eta_{22} \boldsymbol{\phi}_K \end{bmatrix}$$
(2.20b)

for the zero matrix  $\mathbf{0}$  of K by K.

The cross-correlated bivariate random fields of the tensile strength and fracture energy are then given by

$$\chi(\mathbf{x}_i, \boldsymbol{\theta}) = \begin{cases} f_{\mathrm{t}}(\mathbf{x}_i, \boldsymbol{\theta}) \\ G_{\mathrm{f}}(\mathbf{x}_i, \boldsymbol{\theta}) \end{cases} \approx \begin{cases} \exp\left[\tilde{\mu}_1 + \tilde{\sigma}_1 \bar{\chi}_1(\mathbf{x}_i, \boldsymbol{\theta})\right] \\ \exp\left[\tilde{\mu}_2 + \tilde{\sigma}_2 \bar{\chi}_2(\mathbf{x}_i, \boldsymbol{\theta})\right] \end{cases}$$
(2.21)

for the material parameters  $f_t(x, \theta)$  and  $G_f(x, \theta)$  at the point  $x_i$ .

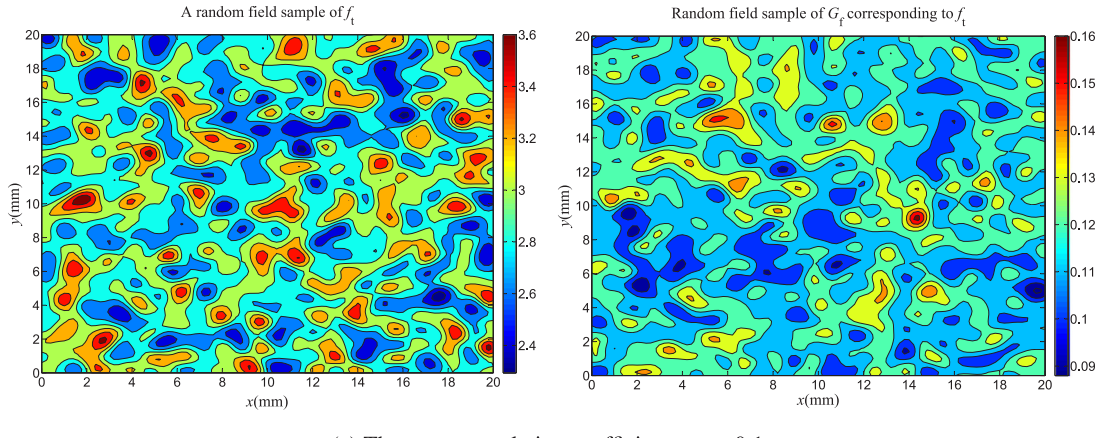
Fig. 3 presents the samples of the failure strength  $f_t$  and the fracture energy  $G_f$  with various correlation coefficients  $\rho_{12} \in (0, 1)$ . It can be observed that as the correlation coefficient increases, the failure strength varies in a more consistent manner with the fracture energy at the same position.

Remark 2.3. For any heterogeneous solid with inhomogeneous micro-structure, the usual mechanical properties on the macroscopic level, e.g., the failure strength  $G_f$  and fracture energy  $f_t$ , etc., become vague in the physical meaning, when they are treated either as random fields or by mesoscopic compositions. However, though the material cannot be treated as a macroscopically homogeneous continuum, the mechanical properties still have definite physical meanings on the mesoscopic level. The above fact justifies the PF-CZM with the phase-field length scale b chosen as an arbitrarily small numerical parameter.  $\Box$ 

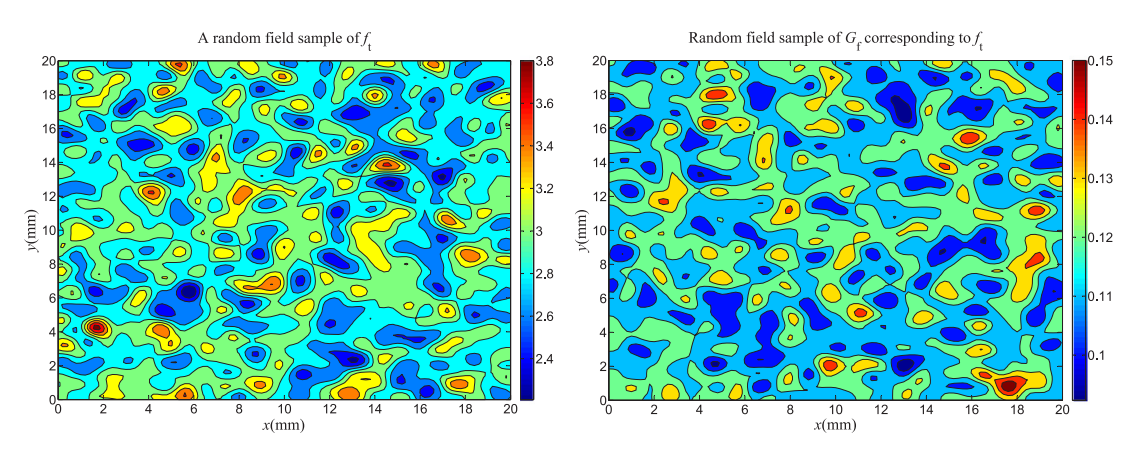
## 2.3. Stochastic and deterministic length scales

The random field representations of material properties naturally introduce an important length scale, i.e. the correlation length  $\ell$ , to the model. The correlation length  $\ell$  characterizes the spatial variation of the mechanical properties over the computational domain. For a specific auto-correlation function  $R_{\bar{\chi}}(\tau)$ , a larger correlation length  $\ell$  indicates a less spatial randomness of the material properties, i.e. the material is more homogeneous. Meanwhile, fracture of quasi-brittle materials is featured by a FPZ of finite size. The length of the FPZ is related to the Irwin characteristic length  $\ell_{\rm ch}$ , whereas the width of FPZ  $\ell_b$  represents another length scale. It has been suggested that  $\ell_b$  can be measured as the minimum possible spacing of parallel cracks when cracks are not localized [57]. The relation between  $\ell$  and  $\ell_b$  has important implications for stochastic modeling of quasi-brittle fracture [19–21]; see Remark 2.4.

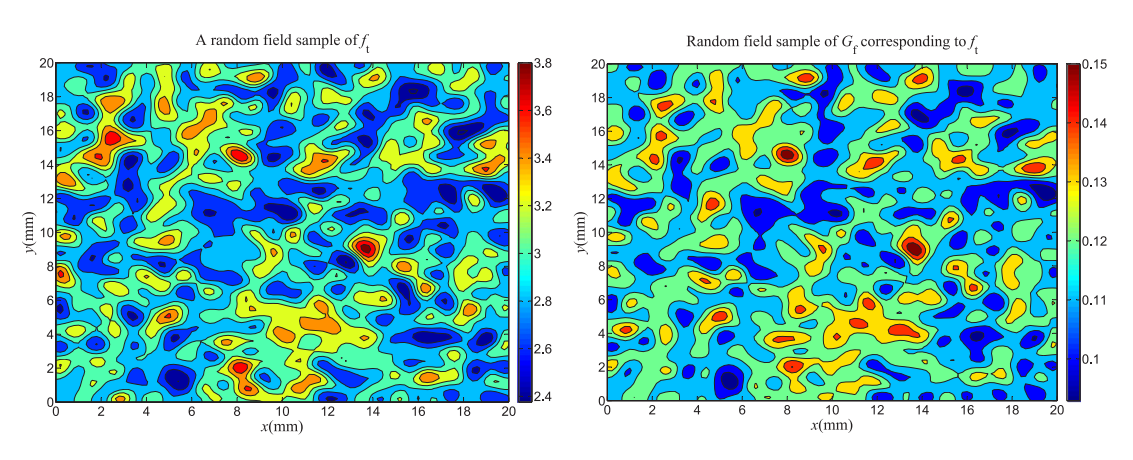
For the PF-CZM introduced in Section 2.1, it is noted that the parameter  $a_1 \propto \ell_{\rm ch}/b$  given in Eq. (2.3) is derived from the 1-D analytical result for homogeneous solids [33]. This implies that, to directly use the model, we consider that the material inside the crack band does not exhibit significant spatial variation of material properties. In other words, the FPZ width  $\ell_b$  is considerably smaller than the correlation length  $\ell$  of the random field. In this case, it is unnecessary to explicitly consider the FPZ width as long as the fracture energy is incorporated. This is exactly



(a) The cross-correlation coefficient  $\rho_{12} = 0.1$ 



(b) The cross-correlation coefficient  $\rho_{12} = 0.5$ 



(c) The cross-correlation coefficient  $\rho_{12} = 0.9$ 

Fig. 3. Samples of the cross-correlated random field  $f_t$  and  $G_f$  with different correlation coefficients  $\rho_{12}$  (Here the parameters  $\mu_1 = 3$  MPa,  $\mu_2 = 0.12$  N/mm and  $\delta_1 = \delta_2 = 0.1$  are adopted). As expected, the larger the cross-correlation coefficient  $\rho_{12}$  is, the failure strength varies spatially in a more consistent trend with the fracture energy.

the case of the PF-CZM, where the length parameter b is a numerical parameter that can be chosen to be arbitrarily small.

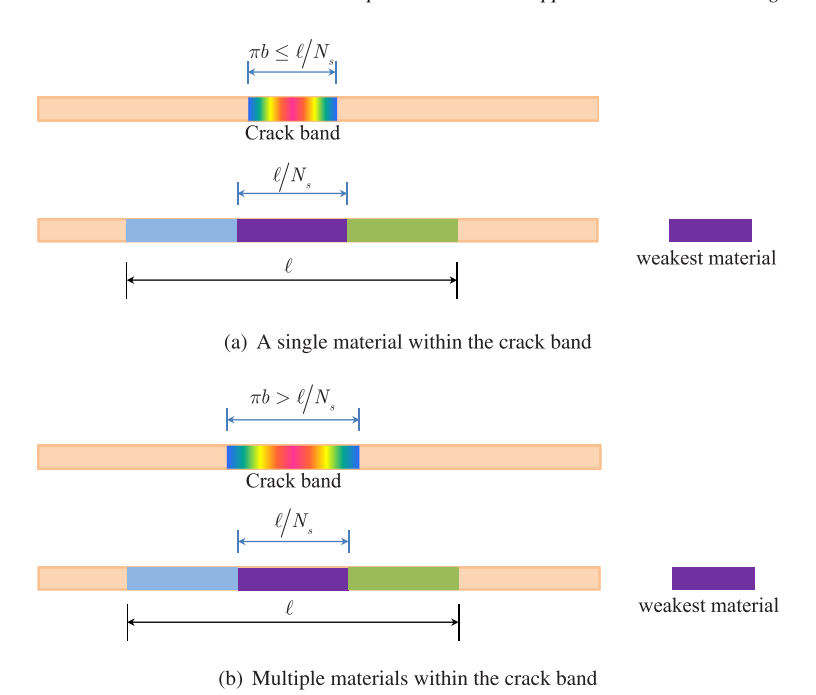


Fig. 4. The upper bound condition between the phase-field length scale parameter b and the correlation length  $\ell$  (here  $N_s = 3$  for illustration). When the condition  $\pi b \le \ell/N_s$  is fulfilled as in Fig. 4(a), only a single material is contained within the crack band such that the latter can be still treated as a macroscopic homogeneous solid; otherwise, several materials co-exist as in Fig. 4(b) and in this case special cares need to be introduced to guarantee objectivity of the stochastic simulation results.

In this study, we specifically require the material in the simulated crack band of width  $\ell_b = \pi b$  to be locally homogeneous. In the context of PF-CZM, this transforms into the following condition

$$\pi b \le \ell/N_s \tag{2.22}$$

where  $N_s$  = parameter such that the spatial randomness of material properties over the distance  $\ell/N_s$  essentially vanishes, and typically  $N_s \approx 2-4$  is adopted. In other words,  $N_s$  represents the number of different materials within the spatial distance of a single correlation length  $\ell$  with its value related to the grid size discretizing the random field; see Section 3.1 for the details. Upon this condition, the FPZ contains only a single material as shown in Fig. 4(a). Otherwise, multiple materials co-exist as in Fig. 4(b), invalidating the model parameter  $a_1 \propto \ell_{\rm ch}/b$  given in Eq. (2.3) for homogeneous solids. Moreover, this is justified and also consistent with Remark 2.3.

Eq. (2.22) imposes an upper bound for the phase-field length scale parameter b. In the PF-CZM, this condition can always be fulfilled for a fixed correlation length  $\ell$  since the length scale b is a numerical parameter that can be arbitrarily small. In this case, the results of the stochastic simulation are insensitive to the length scale parameter and the mesh size; see Sections 4 and 5 for the numerical validation.

**Remark 2.4.** It should be emphasized that the FPZ width  $\ell_b$  represents an essential length scale governing the statistical size effect on the failure behavior. It needs to be explicitly considered in stochastic analyses [19,21], if  $\ell_b$  is not so small compared to the correlation length  $\ell$ . As a consequence, the material properties inside each finite element would unavoidably exhibit considerable spatial randomness. In this case special cares need to be introduced as in the crack band method [20,21] such that objectivity of the numerical stochastic responses with respect to the FE discretization can be guaranteed.

## 3. Numerical implementation

To implement the above computational framework, we first generate the cross-correlated bivariate random field of tensile strength and fracture energy, and the random field is then projected to the finite elements for Monte-Carlo simulation (MCS) of the fracture behavior of the structure.

## 3.1. Generation of sample structures

As discussed in Section 2.2, the cross-correlated bivariate random field of lognormal distribution is generated by the K-L expansion method. For the given probability distribution of the tensile strength  $f_t$  and fracture energy  $G_f$ , the eigenvalues  $\bar{\lambda}$  and eigenfunctions  $\bar{\phi}(x)$  of the correlation function matrix  $C_R$  in Eq. (2.12) are calculated. In accordance with Eq. (2.19) and (2.21), N samples of the cross-correlated bivariate random field of lognormal distribution are generated as the material properties necessary for subsequent finite element simulations.

For the MCS, the random field has to be spatially discretized into stochastic elements and transformed into a set of random variables. In this study, we use the local projection method to map the random field onto the finite element mesh. The strength and fracture energy used for the constitutive behavior of each finite element are extracted by using the values of the underlying random fields at the centroid of the finite element. This mapping method requires that the material properties are almost uniform inside the finite element. The random field is generated over a grid, where the grid size is chosen to capture the essential characteristics of the spatially varied mechanical properties. Previous studies suggested the optimal grid size  $h_s$  for the random field to be in the range  $h_s = \frac{1}{N_s} \ell \le \left(\frac{1}{4} \sim \frac{1}{2}\right) \ell$  [15,58–60]. If the grid size is too large, it will not capture the correlation feature of the random field. If it is too small, there could be numerical instability in decomposing the covariance matrix  $C_{\bar{\chi}}$ .

## 3.2. Finite element analysis

For each sample of the bivariate random field of tensile strength and fracture energy, the governing equations for the PF-CZM are then solved numerically. In order to reduce computational cost, the whole structure can be divided into two sub-domains: the sub-domain  $\mathcal{B}^h$  where the cracks are expected to present and the remainder  $\Omega^h \setminus \mathcal{B}^h$  that is cracking free. Those nodes belonging to the sub-domain  $\mathcal{B}^h$  have degrees of freedom (dofs) of both mechanical displacement and crack phase-field. The element within the sub-domain  $\mathcal{B}^h$  needs to be sufficiently smaller than the length scale b such that an accurate estimation of the fracture energy can be guaranteed [24]. Previous studies [33–35] suggested that the mesh size of finite elements  $h_e \leq \frac{1}{5}b$  is usually sufficient. Accordingly, it follows from the upper bound condition (2.22) that

$$5\pi h_e \le \pi b \le h_s \le \left(\frac{1}{4} \sim \frac{1}{2}\right)\ell\tag{3.1a}$$

or, equivalently,

$$5h_e \le b \le \frac{h_s}{\pi} \le \left(\frac{1}{4} \sim \frac{1}{2}\right) \frac{\ell}{\pi} \tag{3.1b}$$

Comparatively, the nodes within the elastic sub-domain  $\Omega^h \setminus \mathcal{B}^h$  have only displacement dofs and the material is linear elastic, and therefore larger elements can be used.

As the governing equations of the phase-field model are coupled and strongly nonlinear, it is rather challenging to numerically solve the resulting discrete equilibrium equations. In particular, for the MCS involving a large number of deterministic simulations, a robust and efficient solver is needed. In this work, the Broyden–Fletcher–Goldfarb–Shanno (BFGS) monolithic algorithm with consistent stiffness modification is adopted. As extensively verified in [61–65], this monolithic algorithm is much (around 10 times) faster than the alternate minimization (AM) or staggered algorithm [24,34,66] with comparable robustness.

#### 3.3. Monte-Carlo simulations

The MCS is a versatile mathematical tool for the computational modeling of stochastic problems. This method consists of repeatedly generating samples of the random field and then evaluating the statistical characteristics of responses from the deterministic finite element simulations. The advantage of MCS is that it can handle complex problems in a unified manner without relying on analytical solutions. Accuracy of the numerical results can be simply improved by increasing the number of samples. Due to the limitation of computational cost, practically the number of samples is considered to be large enough so long as the first- and second-order statistical characteristics of the stochastic responses, e.g., mean value, standard deviation, etc., converge with an acceptable tolerance. However,

## Algorithm 1: Monte-Carlo simulations using the probabilistic PF-CZM

**Data:** Given statistical parameters of the failure strength  $f_t$  and fracture energy  $G_f$ : The mean values  $\mu$ , the coefficients of variations  $\delta$ , cumulative distribution function  $F_{\chi}(\chi)$ , auto-correlation function  $R_{\chi}(\tau)$  and correlation length  $\ell$ .

#### Create the finite element model

- (a) Discretize the computational domain
- (b) Apply the boundary and loading conditions

## Generating the samples of the random field

- (a) Decompose the correlation function matrix  $C_R$  with the given statistical parameters
- (b) Generate the cross-correlated bivariate random field by the K-L expansion method.

## for every sample structure do

- (a) Assign the random mechanical parameters to the finite elements in the potential damage sub-domain and the mean values to those in the remaining elastic regions, respectively
- (b) Run the finite element simulation of the sample structure using the PF-CZM upon the condition (3.1)

#### end

Analyze the statistical information of the stochastic responses

the required number of samples is usually problem-dependent and has to be determined by trial and error. In the context of the probabilistic PF-CZM this topic will be discussed later in the numerical examples.

Regarding the cross-correlated bivariate random field of lognormal distribution, N number of samples are generated in the MCS by the K-L expansion method. For each sample, the random material parameters are assigned to those finite elements within the region  $\mathcal{B}^h$ , and the mean values of material parameters are given to elements in the remaining elastic region  $\Omega^h \setminus \mathcal{B}^h$ . These regions can be identified based on either the experimental observation or the failure pattern simulated by an *a priori* deterministic model, which uses the mean material properties. The PF-CZM is used to calculate the structural response for each sample of random fields. The statistical information, including the mean, the variance and the probability of the random responses (i.e., crack evolution, load–displacement curve, etc..), is then obtained. A sufficient number of samples are used in the MCS such that the simulated variance of the peak load capacity converges within a relative error of 5%; see Section 4.2 for more details.

The above numerical algorithm of the MCS for the phase-field cohesive zone modeling of stochastic fracture is shown in Fig. 5 and Algorithm 1.

## 4. Numerical verification

In this section, two numerical examples are presented to verify the proposed probabilistic PF-CZM. In particular, we investigate the effects of the length parameters (i.e., phase-field length scale parameter b, correlation length  $\ell$ , mesh size  $h_e$  for finite elements and the grid size  $h_s$  for random field generation) on the simulated fracture behavior (crack patterns, failure modes and global responses). In order to guarantee the mesh objectivity, sufficiently refined quadrilateral bilinear elements ( $h_e \leq b/5$ ) are used to discretize the potential damage sub-domain with random mechanical parameters, while the remaining elastic regions are discretized using triangular or quadrilateral elements of larger mesh sizes with the mean material properties. The plane stress state is assumed in all simulations.

## 4.1. 1-D bar under uniaxial tension

As shown in Fig. 6, a 1-D softening bar of length L = 200 mm and unit cross section under uniaxial traction is considered. The left end of specimen is fixed, and the right end is subjected to an increasing displacement  $u^*$ .

The model parameters are taken from [33]. For this 1-D problem, crack nucleation occurs when the tensile strength of the element is reached and the peak load of the bar is governed only by the tensile strength. Therefore, we consider tensile strength to be the only random variable, with the mean value  $f_t = 3.0$  MPa and the coefficient of variation (CoV)  $\delta_1 = 0.20$ . Other material properties are assumed to be deterministic, i.e., Young's modulus  $E_0 = 30$  GPa, Poisson's ratio  $\nu_0 = 0.20$ , and the fracture energy  $G_f = 120$  J/m<sup>2</sup>.

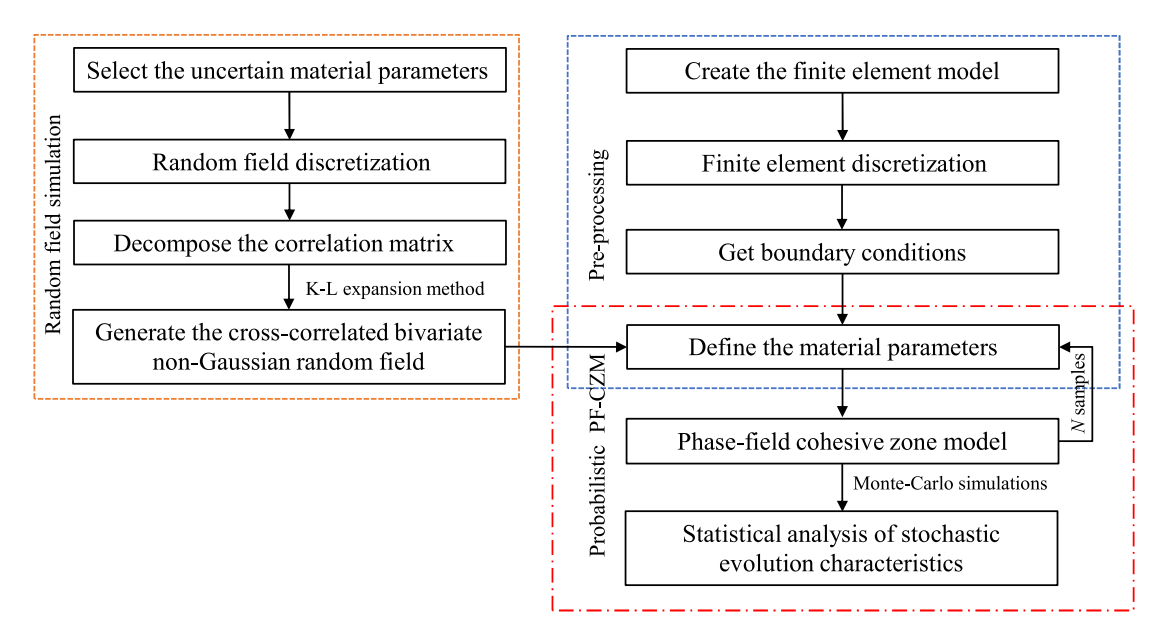


Fig. 5. Flowchart for the Monte-Carlo simulation using the probabilistic PF-CZM.



Fig. 6. 1-D bar under uniaxial traction: Geometry, loading and boundary conditions.

This example uses the linear softening law  $(2.6)_1$ . A total of 500 samples of the random field are generated, and the resulting responses of the bar are numerically simulated by the PF-CZM. For each sample, the minimal value of the tensile strength over the entire specimen is denoted by  $f_{t_{min}}$ . The maximum and minimal values of  $f_{t_{min}}$  in all the 500 samples are denoted by  $\max(f_{t_{min}})$ , and  $\min(f_{t_{min}})$ , respectively. For this 1D problem, it is evident that the peak load of the bar will be attained when the weakest element reaches the its tensile strength. Upon continuing displacement-controlled loading, this element will undergo softening damage, and the remaining part of the bar will undergo unloading. It should be emphasized that the size of the weakest element is equal to the FPZ width,  $\ell_b$ , and, as will be demonstrated later, the tensile strength of this weakest element is not necessarily equal to the minimum value  $f_{t_{min}}$  of the random field of tensile strength.

In the analysis, we fix the grid size  $h_s = \frac{1}{3}\ell = 10$  mm for generation of the random field of  $f_t$ . Four cases of different phase-field length scale parameters, i.e.,  $b = \{30, 10, 10/\pi, 1\}$  mm, and the associated finite element mesh sizes  $h_e = \frac{1}{5}b$ , are considered. In Fig. 7 the simulated  $F^*$  versus  $u^*$  curves are compared against those calculated analytically by prescribing either  $\max(f_{t_{\min}})$  or  $\min(f_{t_{\min}})$  to the strength of the weakest element. Note that the analytical calculation of load-displacement curve does not require the knowledge of  $\ell_b$  as long as the fracture energy  $G_f$  is explicitly introduced.

It is seen from Fig. 7 that, when the FPZ width  $(\ell_b = \pi b)$  is larger than  $h_s$  (Cases I and II), the upper and lower extremes of the simulated load–displacement curves lie above those calculated by using  $\max(f_{t_{\min}})$  and  $\min(f_{t_{\min}})$ , respectively. To explain this result, we note that the peak load of the bar is governed by the minimum tensile strength of all the elements. Since  $\ell_b > h_s$ , the tensile strength  $\bar{f}_t$  of the element can be considered as an average of the input random tensile strength over a distance  $\ell_b$ . Therefore, the minimum value of  $\bar{f}_t$  would be higher than the extreme minimum of the input random field of tensile strength. By comparing Fig. 7(a) and (b), it is found that, as  $\ell_b$  become closer to  $h_s$ , the simulated load–displacement curves move closer to the bounds calculated by  $\max(f_{t_{\min}})$  and  $\min(f_{t_{\min}})$ .

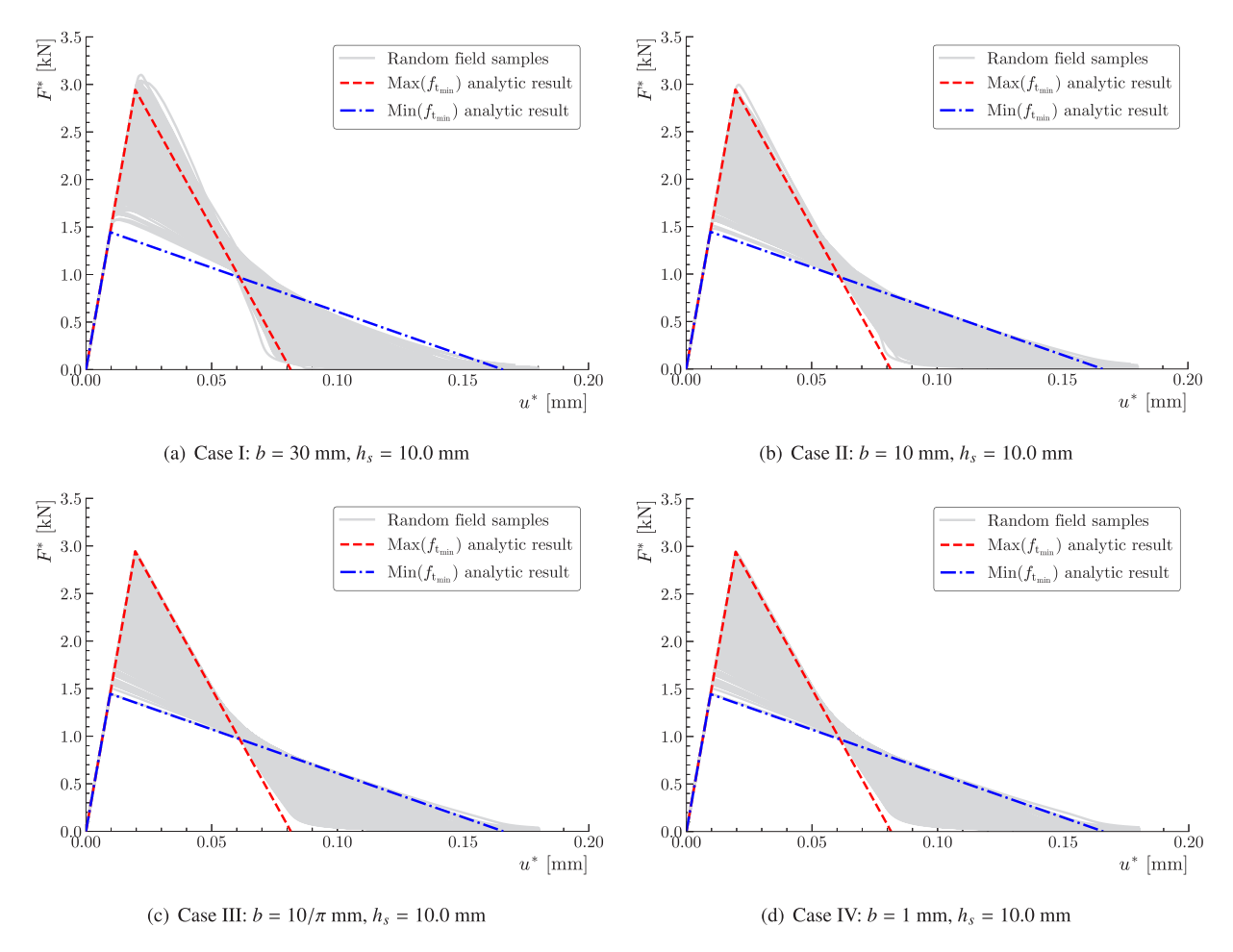


Fig. 7. 1-D bar under uniaxial traction: Load *versus* displacement curves of MCS for various phase-field length scale parameters. In Cases I and II, the FPZ width  $\ell_b$  is larger than the grid size  $h_s$  of the random field generation, the upper and lower extremes of the simulated load–displacement curves lie above those calculated by using  $\max(f_{t_{\min}})$  and  $\min(f_{t_{\min}})$ , respectively. Comparatively, in Cases III and IV,  $\ell_b$  is smaller than  $h_s$ , the load–displacement curves based on  $\max(f_{t_{\min}})$  and  $\min(f_{t_{\min}})$  represent the upper and lower bounds of the stochastic responses.

When the FPZ width is smaller than  $h_s$  (Cases III and IV), the material tensile strength does not exhibit statistical variation within the element. Therefore, the minimum tensile strength of the material element in the bar is equal to  $f_{t_{min}}$ . In this case, the load–displacement curves based on  $\max(f_{t_{min}})$  and  $\min(f_{t_{min}})$  represent the upper and lower bounds of the simulated stochastic load–displacement responses. Note that due to the numerical inaccuracy resulting from the phase-field approximation with a non-vanishing length scale parameter, some deviations from linearity in the tails of the curves are exhibited; see [33] for more discussion.

Fig. 8 presents the simulated cumulative distribution function (CDF) of the peak load  $F_{\text{max}}$ . It is seen that, when  $\ell_b \leq h_s$ , the probability distribution of  $F_{\text{max}}$  is independent of the length scale parameter b. Though damage would localize into a material element of size  $\pi b$ , the strengths of material elements over the distance  $h_s$  is essentially the same. Recent studies used a level excursion analysis to show that in this case the essential length scale governing the probability distribution of the peak load is the correlation length  $\ell$  instead of  $\ell_b$  [67,68]. By contrast, for Cases I and II ( $\ell_b \geq h_s$ ), the CDF of  $F_{\text{max}}$  depends strongly on the choice of b. In this case, the strengths of adjacent material elements exhibit some degree of statistical variations. Therefore, both  $\ell_b$  and  $\ell$  play roles in determining the CDF of  $F_{\text{max}}$ . When the FPZ width is significantly larger than the correlation length, the statistics of  $F_{\text{max}}$  can be described by a finite weakest-link model, in which the FPZ width serves a sole characteristic length scale [19,48,49].

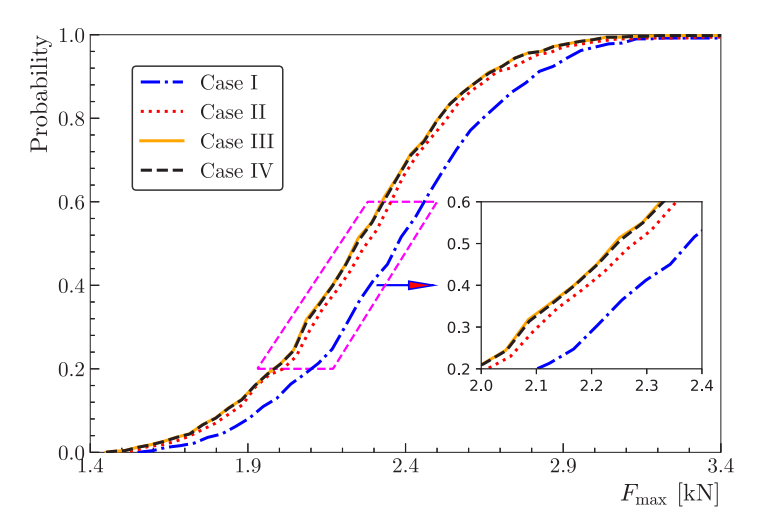


Fig. 8. 1-D bar under uniaxial traction: Probability distributions of the peak load for different phase-field length scale parameters.

The foregoing discussion supports the discussion about the deterministic and stochastic length scales in Section 2.3. Specifically, when the FPZ width is considerably smaller than the correlation length of the random field of tensile strength, the FPZ width does not need to be considered explicitly in the model once the fracture energy is directly incorporated in the model. Accordingly, the length parameter *b* in the PF-CZM can be treated as a numerical parameter. When the FPZ width is not small compared to the correlation length, the FPZ width has to be considered explicitly in addition to the direct incorporation of the fracture energy in stochastic analysis of structural response.

## 4.2. Unnotched concrete beam under three-point bending

The roles of the length parameter b of the PF-CZM and the correlation length are further demonstrated by the simulation of probabilistic failure behavior of the unnotched concrete beam under three-point bending tested by Hoover et al. [69]. As shown in Fig. 9, the specimen has a span of 202 mm, depth of 93 mm, and out-of-plane thickness of 40 mm. To avoid unstable crack propagation in the post-peak regime, the specimen was loaded by the crack mouth opening displacement (CMOD), which is defined by the difference in horizontal displacements of two symmetric points  $C_1$  and  $C_2$  with the gauge span 59 mm. In a previous study [46], the PF-CZM was used for deterministic analysis of this beam. It was shown that the simulation results are insensitive to the phase-field length scale and mesh discretization.

In this study, we analyze the fracture behavior of the beam in a probabilistic setting. A bivariate random field of lognormal distribution with CoVs  $\delta_1 = \delta_2 = 0.15$  is used to describe the randomness in the cross-correlated tensile strength  $f_t$  and fracture energy  $G_f$ . The correlation coefficient  $\rho_{12}$  between  $f_t$  and  $G_f$  is assumed to be 0.5. The mean values of these parameters and other deterministic mechanical properties are taken from [46] and listed in Fig. 9. The Cornelissen et al. [37] softening curve  $(2.6)_2$  is used for concrete.

The previous deterministic analysis showed that the failure of this unnotched beam is featured by the initiation and propagation of a mode I crack at the center of the bottom surface [46]. In probabilistic analysis, due to the spatial randomness of strength and fracture properties, there is no guarantee that the crack will initiate at the mid-span and propagate vertically upwards. Nevertheless, due to the stress field, it is expected that the damage would occur around the mid-span region. Therefore, in order to reduce the computational cost, only the middle region of sizes 40 mm  $\times$  93 mm is selected as the damage sub-domain with random mechanical properties and the remaining part of the specimen is considered to be elastic with deterministic material parameters. The correlation length  $\ell$  is chosen to be 30 mm, and the grid size  $h_s$  for random field is 10 mm. The 1-D numerical results presented in Section 4.1 indicate that, the phase-field length scale and finite element mesh discretization have negligible effects on the stochastic fracture behavior provided the condition  $\pi b \leq h_s$  is fulfilled. To confirm this conclusion, we consider five cases

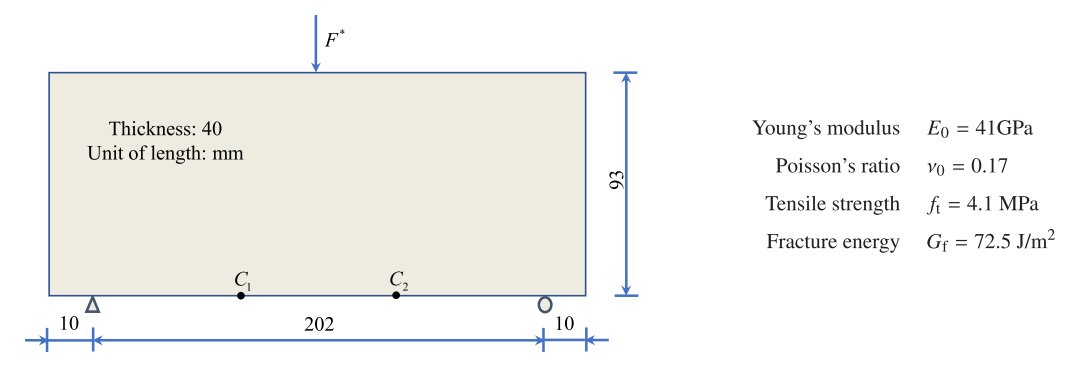


Fig. 9. Unnotched concrete beam under three-point bending: Geometry, loading, boundary conditions and material parameters.

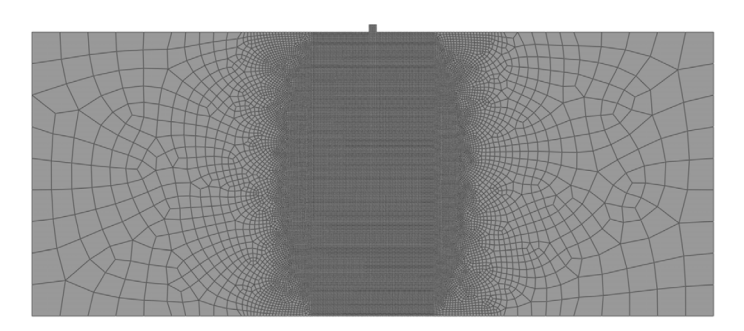


Fig. 10. Unnotched concrete beam under three-point bending: Finite element discretization.

Table 1
Unnotched concrete beam under three-point bending: Five cases with different length scale parameters and finite element mesh sizes.

Cases	Phase-field length scale parameter b (mm)	Finite element mesh size $h_e$ (mm)
I	1.0	0.20
II	1.0	0.05
III	1.0	0.10
IV	1.5	0.10
V	2.0	0.10

listed in Table 1 with various phase-field length scale parameters b and different finite element mesh sizes  $h_e \leq \frac{1}{5}b$  within the damage sub-domain, all satisfying the condition  $\pi b \leq h_s$ ; see Fig. 10 for the finite element mesh of Case I.

One important feature of stochastic analysis is that it can simulate different probable crack patterns or even failure modes. In this example, the crack predicted by deterministic analysis always nucleates at the middle of the bottom surface, where the principal tensile stress is maximum and propagates vertically upwards; see the first column of Fig. 11. By contrast, stochastic simulations predict some variations in the crack pattern, as shown in the second and third columns of Fig. 11. It is seen that a single crack nucleates from the central region of the bottom surface, but not exactly at the mid-span. The crack propagates upward along a zig-zag path to the top surface. The deviation from the deterministic analysis arises from the spatial randomness of material properties. Nevertheless, as in the deterministic analyses, for a given sample of random fields of tensile strength and fracture energy, the predicted crack path is not affected by the phase-field length scale nor the finite element mesh when the condition  $\pi b \leq h_s$  is fulfilled.

For Case I, a total of 1000 samples of random fields were generated for fracture simulations. Fig. 12 compares the simulated force  $F^*$  versus CMOD against the test data [69]. Though we did not calibrate the model parameters, most of the simulation results fall inside the experimental bounds. It is interesting to note that the mean response

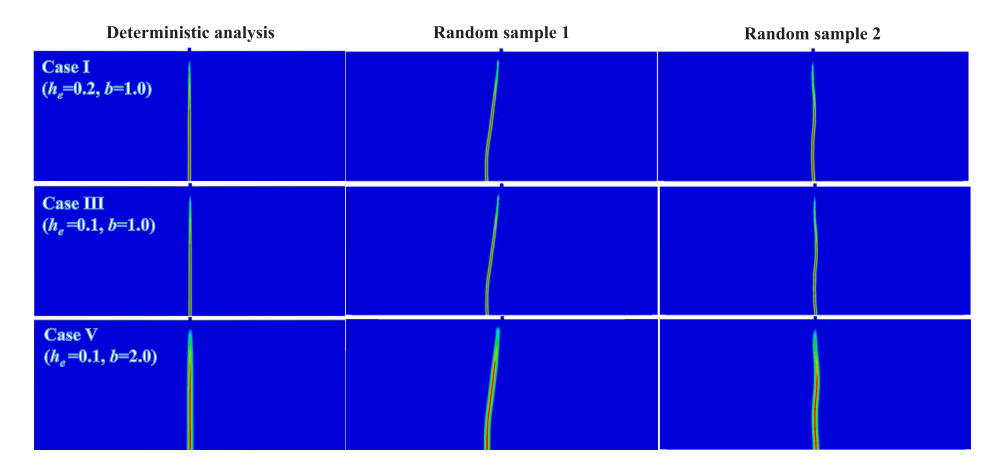


Fig. 11. Unnotched concrete beam under three-point bending: Simulated crack patterns for various length scales. Left column: Crack paths given by deterministic analyses; Middle column: Crack paths given by random sample 1; Right column: Crack paths given by random sample 2.

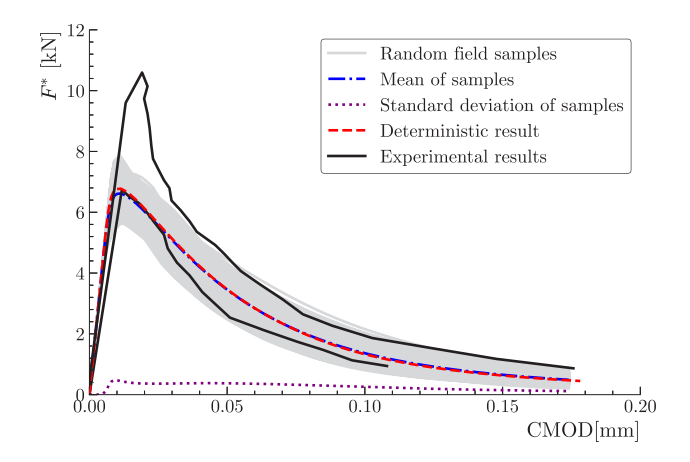


Fig. 12. Unnotched concrete beam under three-point bending: Simulated load versus CMOD curves for Case I ( $h_e = 0.2$  mm, b = 1.0 mm).

calculated from the MCS is very close to the deterministic result using the mean values of the mechanical properties. This can be attributed to the fact that the geometry and loading configuration dictate the initial non-uniform stress field. The spatial randomness of tensile strength and fracture energy is not significantly large as compared to the non-uniformity of the stress field. Therefore, the various probable crack patterns predicted by the MCS are fluctuating around from the deterministic result, but the fluctuation is not significant.

The MCS of 1000 samples are rather time-consuming. It is thus useful to determine the minimal number of samples to achieve the balance between the numerical accuracy and computational cost. To this end, the mean and standard deviation of the peak load are depicted in Fig. 13 for different numbers of sample size. It is seen that, as the number of the MCS increases to around 500, both the first- and second statistical moment converge with a relative difference less than 5%. Therefore, we use 500 samples for MCS for other cases. Fig. 14 compares the simulated load *versus* CMOD curves against the test data. The global responses predicted from these cases are very similar to Case I. The mean and standard deviation of the global responses for all the five cases are depicted in Fig. 15. As seen, the stochastic responses are also insensitive to the phase-field length scale parameter *b* and the finite element mesh discretization.

Fig. 16(a) presents the predicted CDFs of the peak load  $F_{\text{max}}$  for cases I-V. It is seen that the CDF of  $F_{\text{max}}$  is insensitive to the length parameter b. As a comparison, we consider the same cases listed in Table 1 but with a different random field grid size,  $h_s = 0.2$  mm. In these cases, the condition  $\pi b \le h_s$  is violated. The predicted

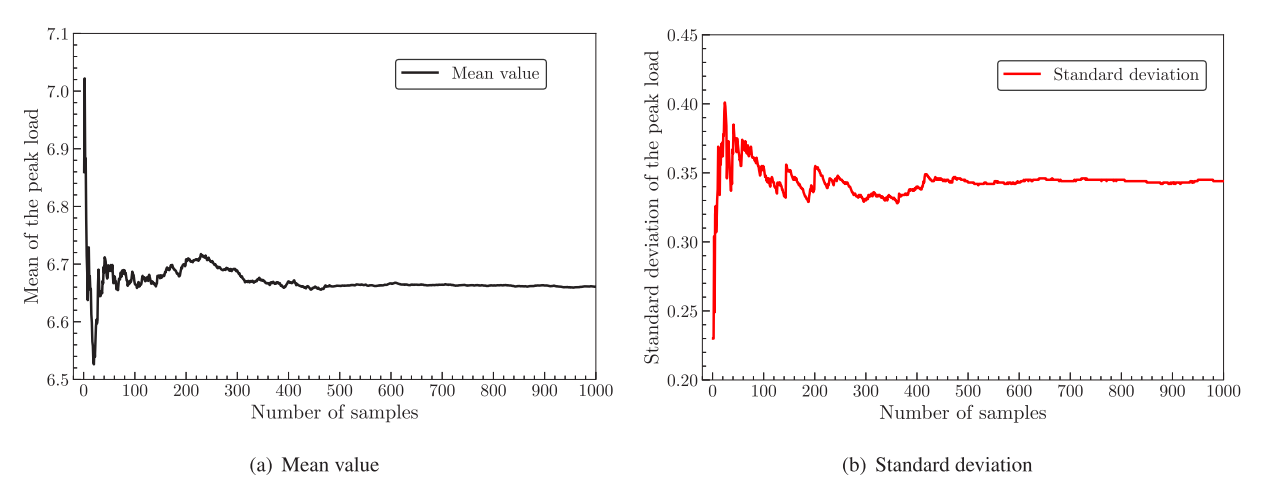


Fig. 13. Unnotched concrete beam under three-point bending: The mean and standard deviation of the peak load (Case I).

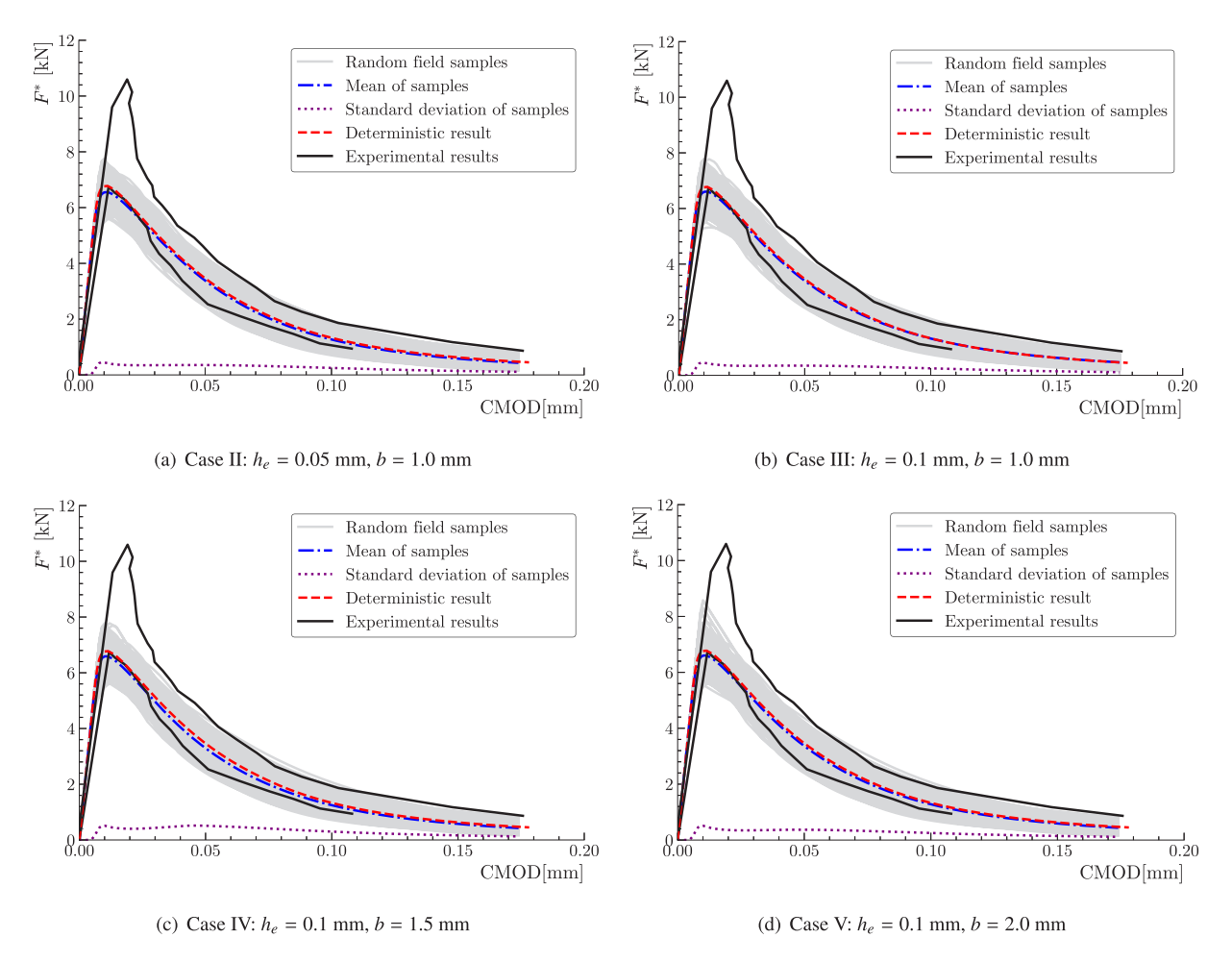


Fig. 14. Unnotched concrete beam under three-point bending: Simulated load versus CMOD curves (case II-V).

CDFs of the peak load are shown in Fig. 16(b). It is seen that the CDF of  $F_{\text{max}}$  now depends on parameter b, which indicates that in such cases the phase-field length parameter needs to be specified as a physical parameter.

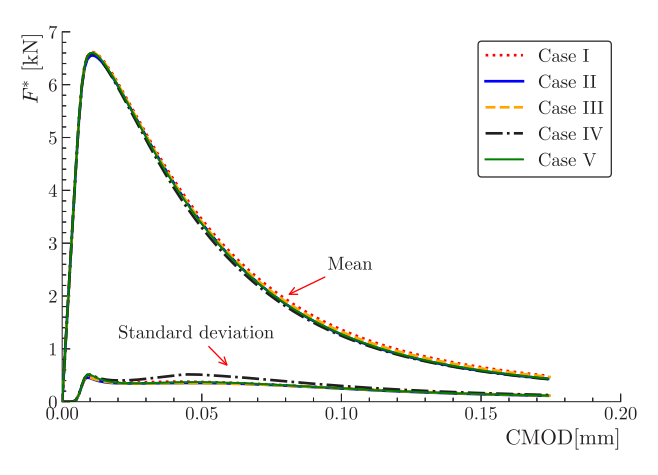


Fig. 15. Unnotched concrete beam under three-point bending: Mean and standard deviation of the load versus CMOD curves.

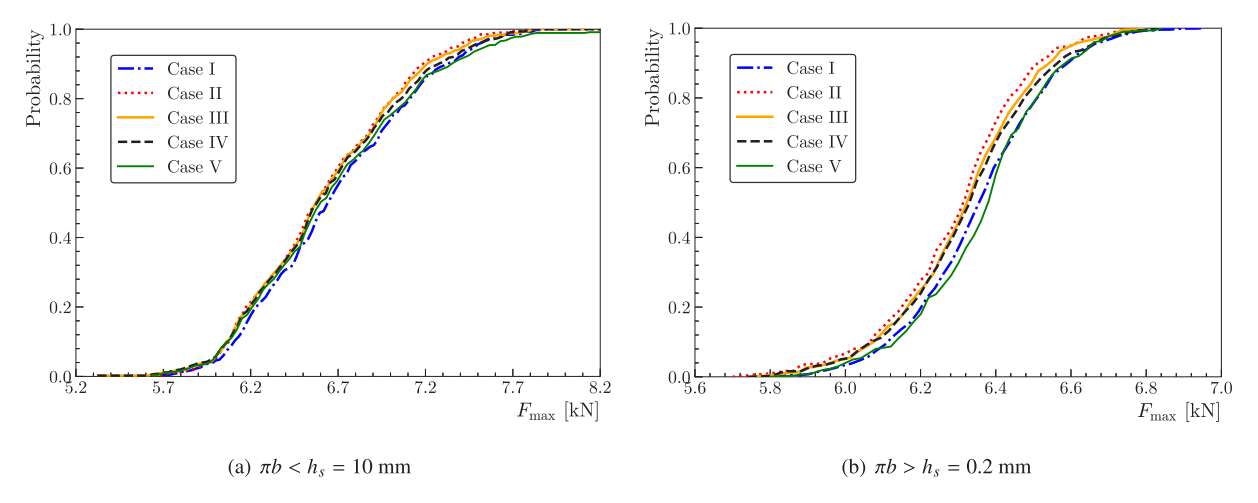


Fig. 16. Unnotched concrete beam under three-point bending: Calculated probability distributions of the peak load.

## 5. Numerical examples

Once verified, the probabilistic PF-CZM is now applied to three numerical examples: (1) a 2-D concrete specimen under uniaxial tension, (2) an unnotched concrete beam under four-point bending, and (3) pull-out of anchor bolt from a concrete plate. In the first two examples, there exists a large region in the specimen where the initial stress field is uniform. Therefore, there is a large uncertainty in the location of crack nucleation and propagation, a scenario that stochastic analysis is needed to understand the various probable failure patterns. The third example illustrates an important practical problem in structural engineering. The concrete plate exhibits an asymmetric cracking pattern even though the structure is symmetric. Such a behavior cannot be predicted by deterministic analysis.

Similar to the verification studies, the cross-correlated bivariate random field of the lognormal distribution with the auto-correlation function  $R_{\chi}(\tau)$  of Gaussian type (2.11) is used to describe uncertainties in the failure strength  $f_{\rm t}$  and fracture energy  $G_{\rm f}$ . Refined quadrilateral bilinear elements satisfying the condition (3.1) are used to discretize the damage sub-domain with random mechanical parameters, while the remaining elastic region is discretized into triangular or quadrilateral elements of larger sizes with the mean material properties. The Cornelissen et al. [37] softening curve (2.6)<sub>2</sub> for concrete and plane stress state are adopted in all simulations.

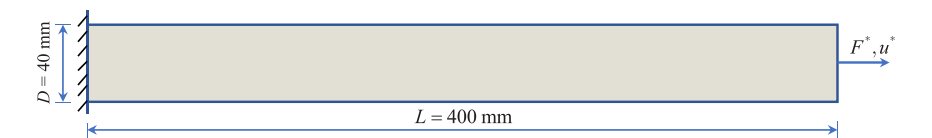


Fig. 17. 2D analysis of concrete bar under uniaxial tension: Geometry, loading and boundary conditions.

**Table 2**2D analysis of concrete bar under uniaxial tension: Different phase-field length scale parameters and finite element mesh sizes.

Cases	Phase-field length scale parameter b (mm)	Finite element mesh size $h_e$ (mm)
I	2.0	0.40
II	2.5	0.40
III	2.5	0.50

## 5.1. 2-D analysis of concrete bar under uniaxial tension

This example is concerned about a 2-D concrete specimen under uniaxial traction. As shown in Fig. 17, the specimen is of length L=400 mm and of cross section 40 mm  $\times$  40 mm. The left end of the specimen is fixed, and the right end is stretched by a monotonically increasing displacement  $u^*$ . A bivariate random field of lognormal distribution is used to represent the cross-correlated tensile strength and fracture energy with the mean values  $f_t = 3.0$  MPa and  $G_f = 120$  J/m<sup>2</sup>; the CoVs of both  $f_t$  and  $G_f$  are  $\delta_1 = \delta_2 = 0.20$ , and the correlation coefficient  $\rho_{12} = 0.5$ . The other mechanical properties, i.e., Young's modulus  $E_0 = 30$  GPa and Poisson's ratio  $\nu_0 = 0.2$ , are treated as deterministic values.

A correlation length  $\ell=30$  mm is used in the simulation with the random field grid size  $h_s=10$  mm. As the crack may nucleate anywhere, in the numerical simulation the whole specimen is discretized into uniformly refined quadrilateral bilinear elements with the aforementioned random material properties. We consider three cases listed in Table 2 with various phase-field length scale parameters b (all satisfying the condition  $\pi b \leq h_s$ ) and finite element mesh sizes  $h_e < \frac{1}{5}b$ .

For the deterministic analysis, as the stress field is uniform and the mechanical properties are homogeneous in the whole specimen, a vertical crack can nucleate anywhere under uniaxial stretching. Numerically, the damage boundary condition d=0 is imposed to the nodes located on both edges such that a vertical crack forms at an interior location (due to round-off errors) as shown in Fig. 18(a). By contrast, in stochastic analysis, due to the presence of randomness in the mechanical properties, the crack, once formed, may not propagate vertically through the depth of the specimen as in the deterministic analysis. Rather, various crack patterns are observed from the MCS; see Figs.  $18(b) \sim 18(d)$  for some typical ones. For instance, a single crack can form at a random location as in Fig. 18(b), but the crack path is no longer vertical since the weakest elements are randomly distributed in the specimen. A second crack pattern is shown in Fig. 18(c), where a major crack and a secondary crack form in the specimen, but the latter one grows only a little bit and then stops. In Fig. 18(d), two primary cracks nucleate: one at the bottom surface and the other at the top surface, and they propagate simultaneously to the opposite surfaces. Fig. 18(e) collects the crack patterns predicted from 50 samples. As expected, the crack can nucleate randomly at any place and the crack paths are mostly tortuous. Such diverse crack patterns have been frequently observed in the test of concrete specimens, yet they cannot be reproduced by deterministic simulations.

Fig. 19 presents the load *versus* displacement curves simulated from the MCS of 500 random samples. The crack pattern shown in Fig. 18(b) occurs in specimens which exhibit a load–displacement curve with steepest softening regime. These specimens have a more brittle behavior since the failure is caused by the propagation of a single crack. The specimens exhibiting a crack pattern shown in Fig. 18(c) tend to have a more ductile post-peak response of the load–displacement curve. The specimens that experience a crack patten depicted by Fig. 18(d) usually exhibit a higher peak load and a more gentle softening post-peak behavior. It is worth noting that, different from the results of three-point bend beam in Section 4.2, the mean value of the peak load predicted by the stochastic analysis is significantly lower than that calculated from deterministic analysis. This behavior can be explained by the weakest-link effect in a probabilistic setting [19]. Therefore, in this case stochastic analysis is needed even for the purpose of predicting the mean behavior.

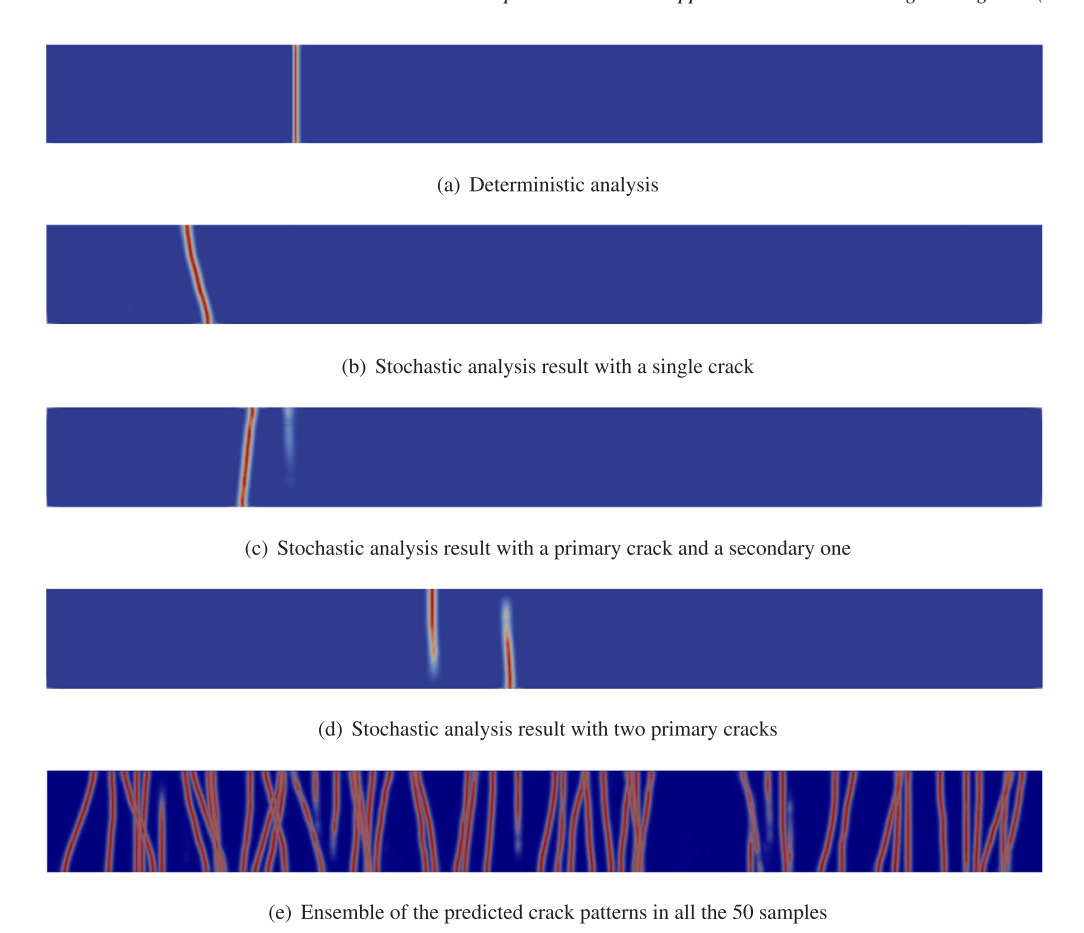


Fig. 18. 2D analysis of concrete bar under uniaxial tension: Simulated crack patterns (Case I).

Fig. 19(d) presents the numerically predicted CDFs of the peak load  $F_{\text{max}}$  from all the three cases. As can be seen, so long as the condition  $\pi b \leq h_s$  is fulfilled, the stochastic responses predicted by the PF-CZM are insensitive to the phase-field length scale parameter and the finite element mesh.

## 5.2. Unnotched concrete beam under four-point bending

The second numerical example considers an unnotched concrete beam under four-point bending. The specimen has a span of 450 mm, a depth of 100 mm and an out-of-plane thickness 50 mm (Fig. 20). Two concentrated forces are applied vertically downward at two points trisecting the span via two monotonically increasing displacements  $u^*$ . The relative displacement between two symmetric points  $C_1$  and  $C_2$  at a gauge length 200 mm (also denoted as CMOD for the sake of simplicity) is monitored during the subsequent analysis. The statistics of the random fields of tensile strength and fracture energy are the same as those used in the foregoing analysis of uniaxial tension specimen. The mean values of tensile strength and fracture energy and other deterministic material parameters are also given in Fig. 20.

In the simulations, the middle region of sizes 170 mm  $\times$  100 mm is selected as the potential damage sub-domain and discretized into quadrilateral elements of uniform sizes, which is modeled by the PF-CZM with the random mechanical properties, while the remaining part of the specimen is assumed to be elastic with the deterministic elastic modulus and Poisson's ratio. The correlation length  $\ell=30$  mm and the random field grid size  $h_s=10$  mm are used as before. As listed in Table 3, three cases with various phase-field length scale parameters b (all satisfying the condition  $\pi b \leq h_s$ ) and different finite element mesh sizes  $h_e \leq \frac{1}{5}b$  are considered for the damage sub-domain.

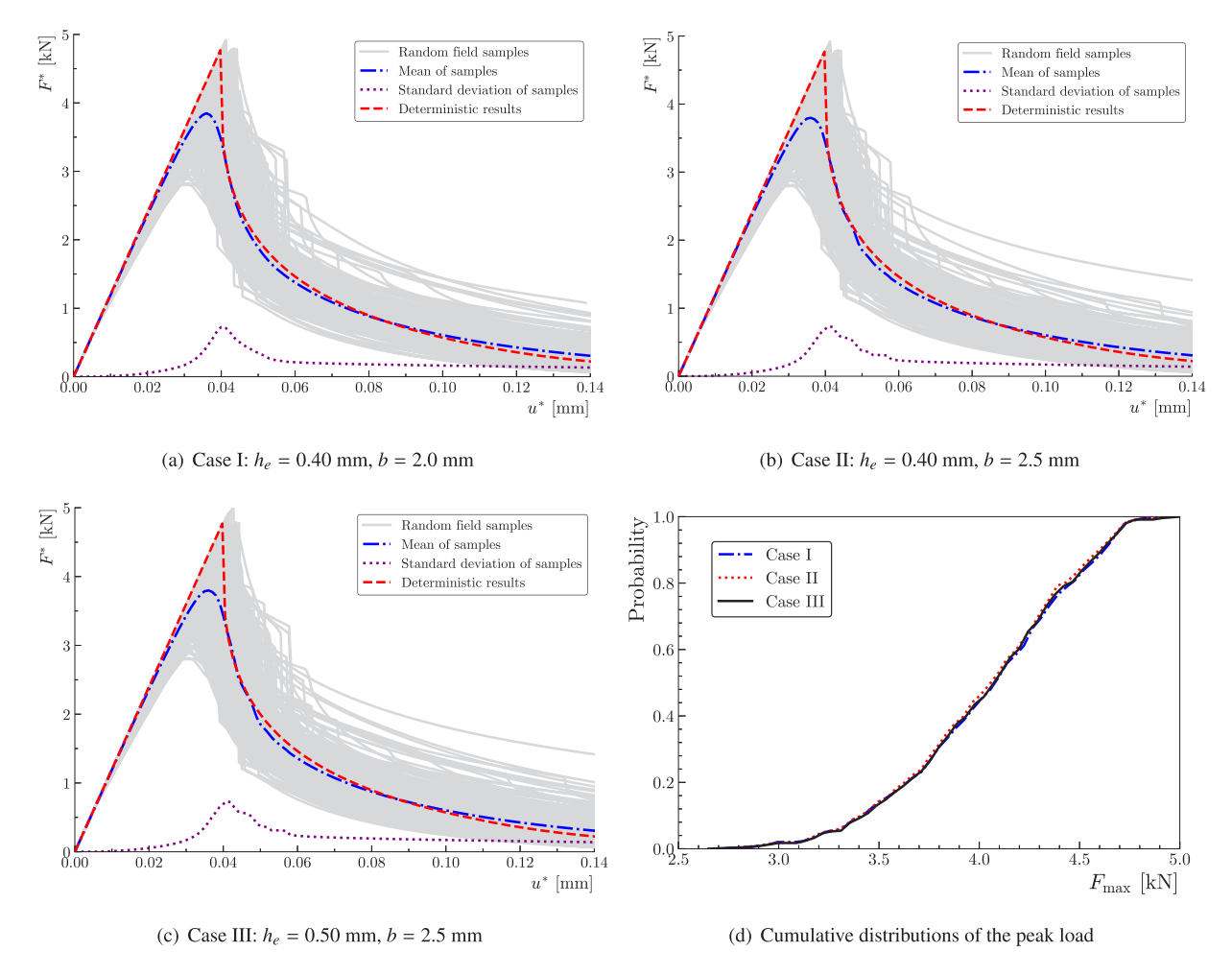


Fig. 19. 2D analysis of concrete bar under uniaxial tension: Load *versus* displacement curves and probability distribution of the peak load calculated by MCS and deterministic analysis.

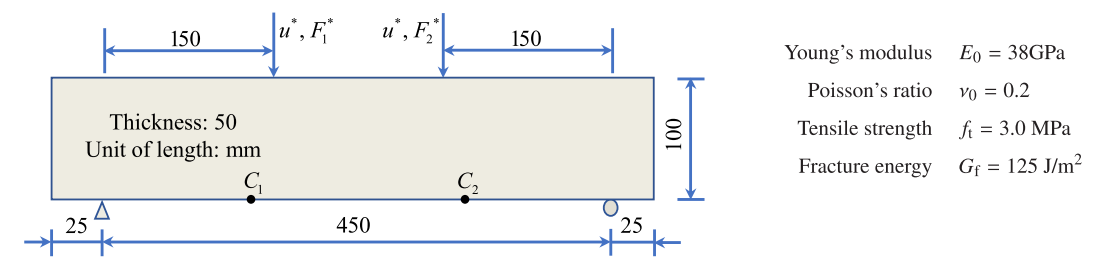


Fig. 20. Unnotched concrete beam under four-point bending: Geometry, boundary, loading conditions, and material parameters.

The specimen is loaded by two equal displacements  $u^*$  at the loading points, and the sum of the resulting forces  $F_1^*$  and  $F_2^*$  is denoted by  $F^*$  in the stochastic analysis.

As both the structure geometry and loading conditions are symmetric, the deterministic analysis usually predicts two symmetric crack propagating vertically to the top surface of the beam as shown in Fig. 21(a), unless distortions are introduced to the finite element mesh to break the symmetry. By contrast, in stochastic analysis the symmetry is broken and cracks can nucleate at any position with weakest failure strengths, even though the initial stress field in

**Table 3**Unnotched concrete beam under four-point bending: Three cases with different phase-field length scale parameters and finite element mesh sizes.

Cases	Phase-field length scale parameter b (mm)	Finite element mesh size $h_e$ (mm)
I	2.0	0.25
II	2.0	0.40
III	2.5	0.40

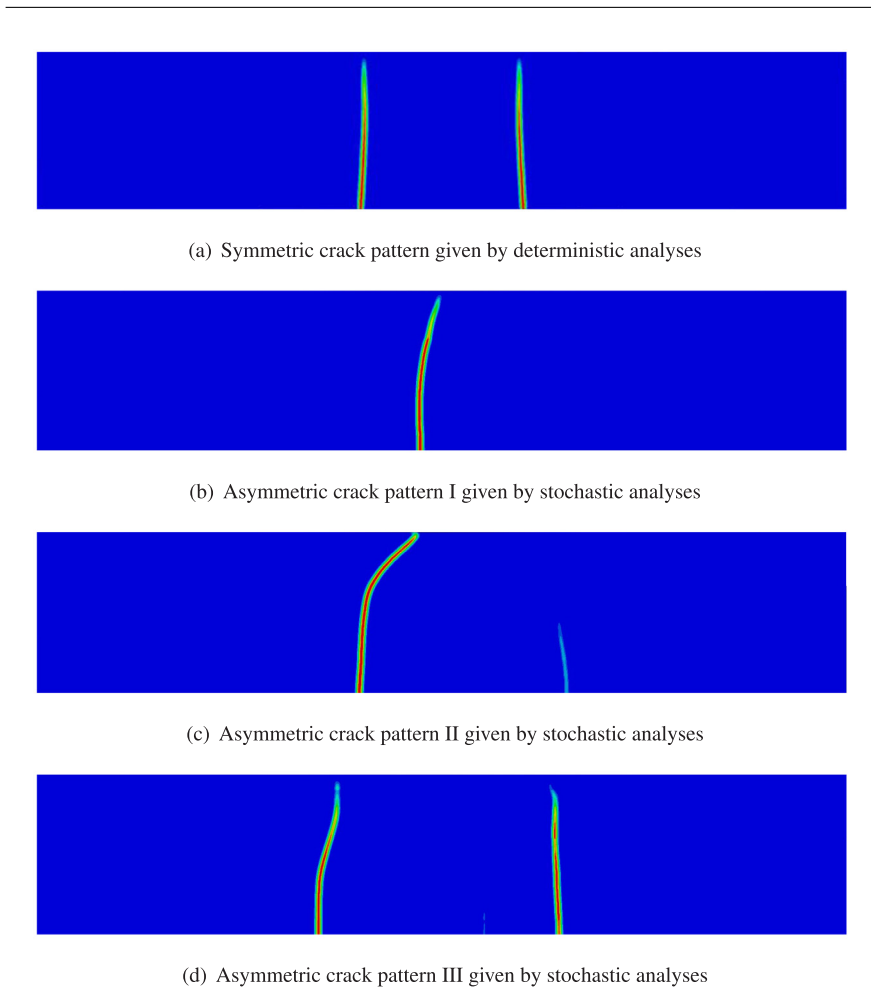


Fig. 21. Unnotched concrete beam under four-point bending: Simulated crack patterns (Case II).

the region of constant moment is uniform. As shown in Fig. 21 (b–d), the beam can exhibit different crack patterns, including a single crack, a primary crack and a secondary one, and two primary cracks.

The numerical load *versus* CMOD curves calculated from the MCS of a total of 500 samples are presented in Fig. 22. Similar to those in the 2-D specimen under traction, various crack patterns lead to different peak loads and softening regimes, thus resulting in distinct global responses. As expected, the more the cracks form and the more tortuous the crack path is, the higher peak load and the more ductile post-peak regime is. Similar to the uniaxial traction discussed in Section 5.1, the mean load *versus* CMOD curves predicted by the stochastic analysis is lower than that predicted by the deterministic analysis. However, the difference between the mean peak load and the deterministic value in this case is smaller than the difference seen in the uniaxial traction case. This is because the uniaxial tension specimen has a larger uniform stress region compared to the four-point bending specimen.

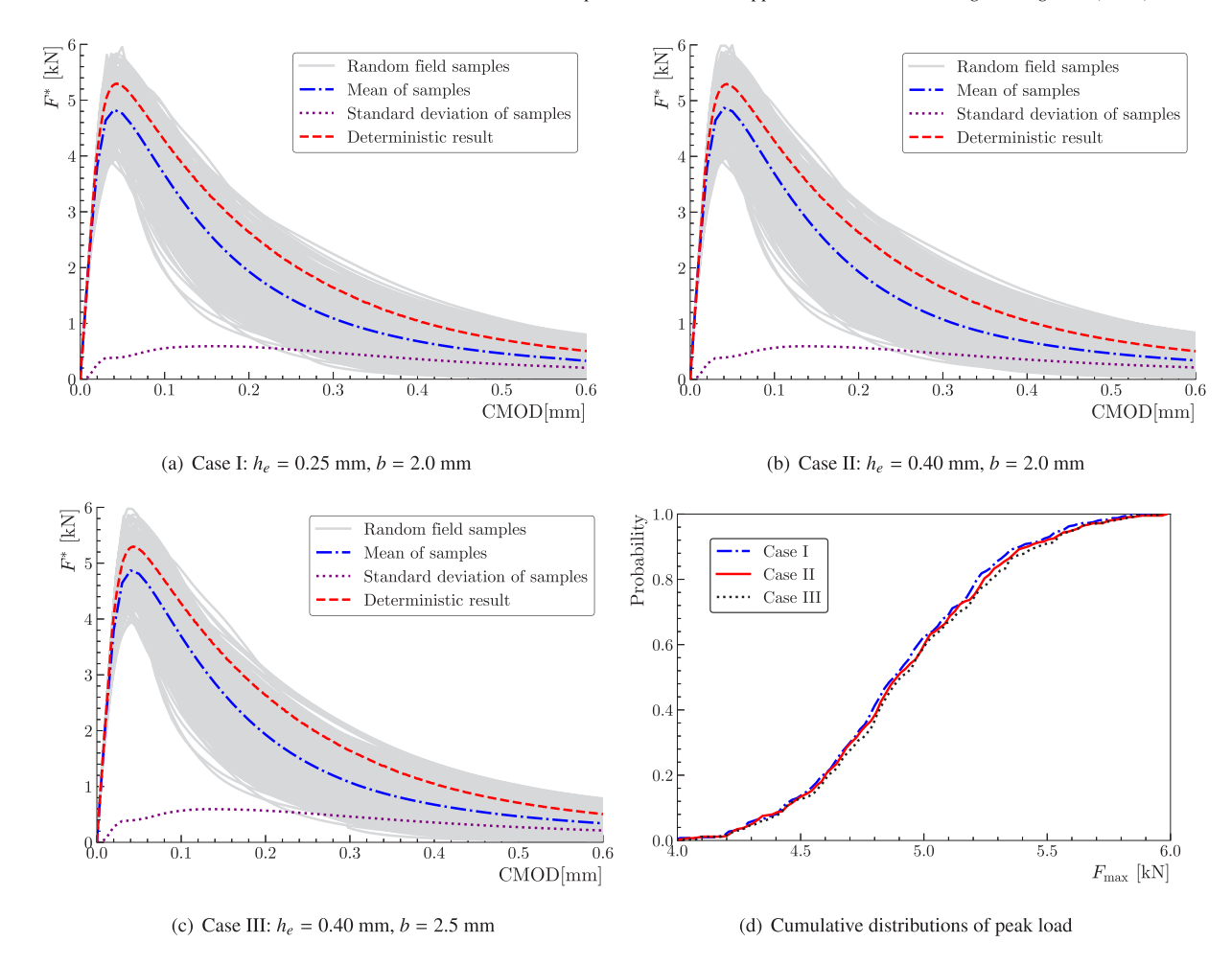


Fig. 22. Unnotched concrete beam under four-point bending: Load versus CMOD curves and probability distribution of the peak load simulated by MCS and deterministic analysis.

Consequently, the four-point bending specimen will exhibit a milder weakest-link effect such that the difference in the mean peak loads predicted by the stochastic and deterministic analyses is smaller.

Remarkably, as shown in Fig. 22(d), the predicted CDF of the peak load  $F_{\text{max}}$  is insensitive to both the phase-field length scale parameter and the finite element mesh discretization so long as the condition  $\pi b \leq h_s$  is satisfied.

## 5.3. Pull-out of anchor bolt from concrete plate

The last example is concerned with the pull-out failure of an anchor bolt from a concrete plate, which was experimentally tested by Vervuurt et al. [70] and reported by Vervuurt et al. [71] in the RILEM Technical Committee 90-FMA. This test has been simulated recently by deterministic analysis [72,73] and stochastic analysis [74–76].

As shown in Fig. 23(a), a T-shaped steel anchor is embedded in a concrete plate with an embedded depth of 150 mm, and the concrete square plate is of length 900 mm and out-of-plane thickness 100 mm. Two supports are devised on the top of concrete panel to prevent the rigid motions. The span of support is 300 mm. As the vertical load  $F^*$  applied upward to the center of an anchor-tail increases, cracks would develop in the concrete plate and consequently the anchor is pulled-out from the specimen. In order to simplify the modeling of the structure and the computation process, in the numerical simulation the contact between the both sides of anchor-head and concrete is assumed to be fully bonded to each other, while other contacts are ignored [75]; see Fig. 23(b).

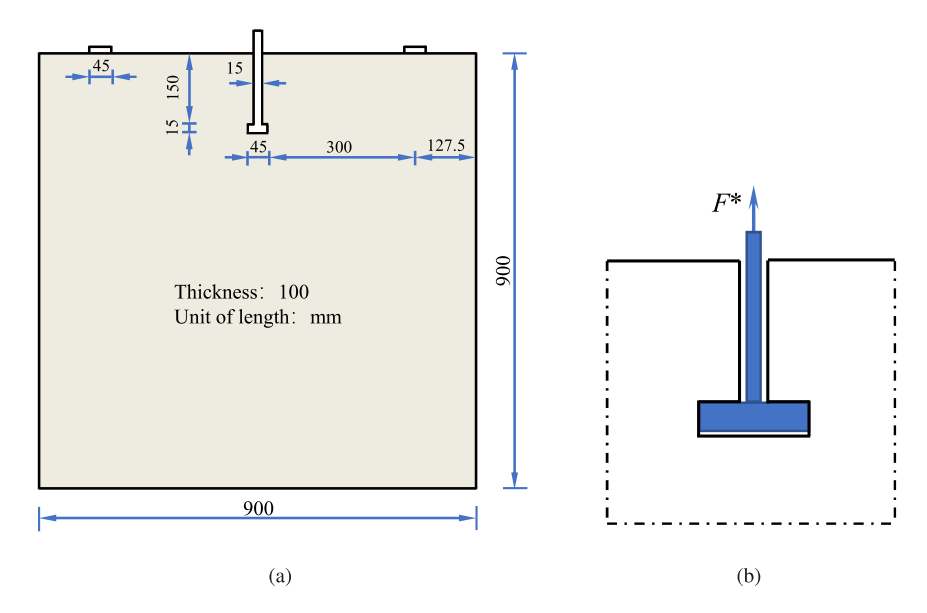


Fig. 23. Pull-out of an anchor bolt from concrete plate: (a) geometry (b) loading condition.

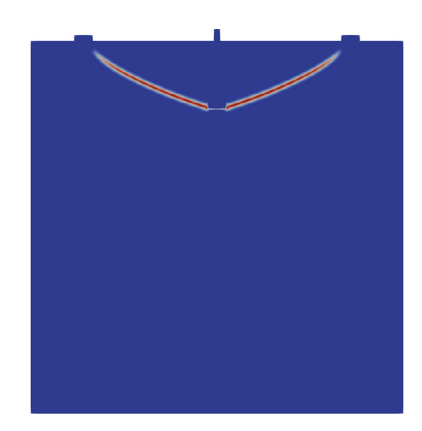


Fig. 24. Pull-out of an anchor bolt from concrete plate: Symmetric crack pattern predicted by the deterministic analysis.

The mean values of the material properties are taken from [70], i.e., Young's modulus  $E_0 = 30$  GPa, Poisson's ratio  $v_0 = 0.2$ , tensile strength  $f_t = 3.0$  MPa and fracture energy  $G_f = 100$  J/m<sup>2</sup>. The spatial randomness of the tensile strength and fracture energy is described by a lognormal bivariate cross-correlated random field. The statistics of the random field are identical to those used in the previous two numerical examples.

In order to reduce the calculation cost, the upper concrete plate of dimensions 900 mm  $\times$  300 mm is selected as the damage-subdomain with random mechanical properties, while the remaining part is assumed to be elastic with deterministic material properties. In this example, the correlation length  $\ell$  and the random field grid size  $h_s$  are taken to be 60 and 24 mm, respectively. The phase-field length scale parameter b=7.5 mm (satisfying the condition  $\pi b \leq h_s$ ) and the mesh size  $h_e=b/5=1.5$  mm are considered in the damage sub-domain.

As shown in Fig. 24, the deterministic analysis predicts a symmetric conical crack pattern in this pull-out test. However, asymmetric failure modes were observed in the test [70,71]: the specimens test-10G028, test-02G003 and test-07G017 exhibited three typical asymmetric crack patterns in Fig. 25. Cracks nucleate at both sides of anchor-head and propagate further, rather irregularly, to the left or right fixing support and edge of plate.

In stochastic analysis, the symmetry of structure is broken by incorporating random mechanical properties. As shown in Fig. 26, various crack patterns are predicted by the probabilistic PF-CZM. Fig. 26(a) shows that the asymmetric crack propagates from one side of the anchor-head towards the fixing support while on the opposite

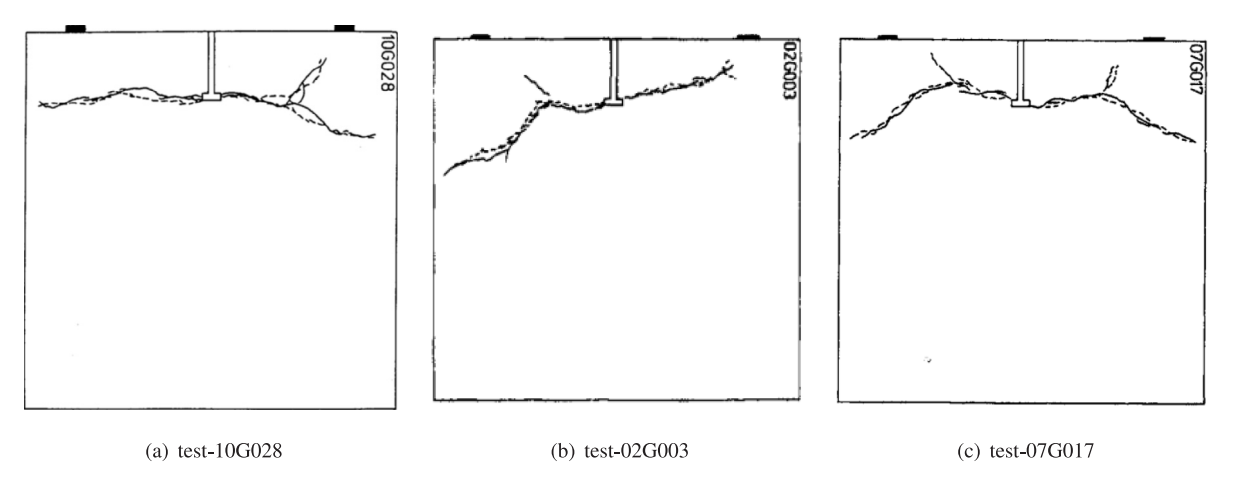


Fig. 25. Pull-out of an anchor bolt from concrete plate: Experimentally observed crack patterns.

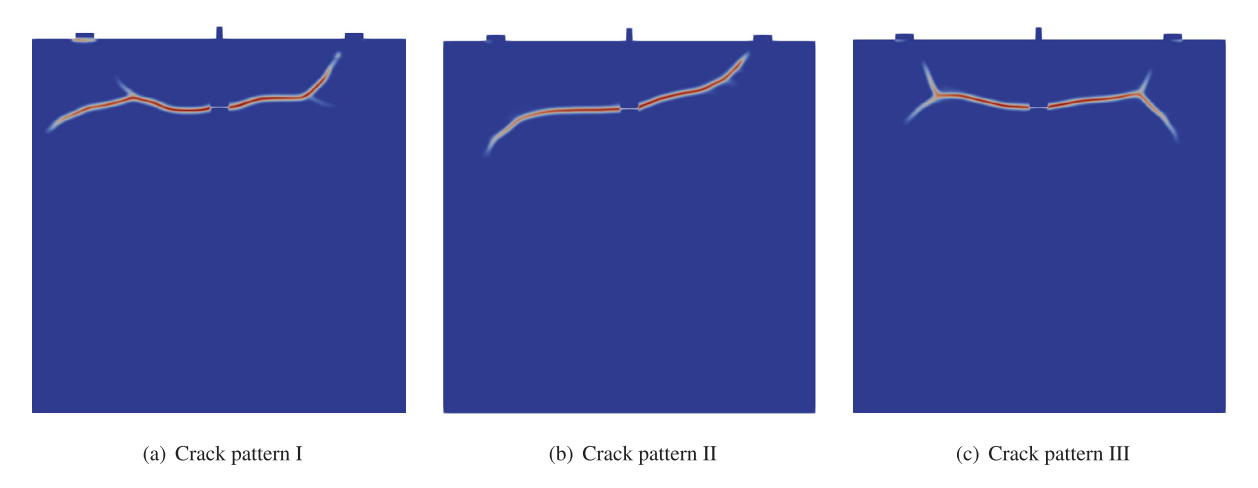


Fig. 26. Pull-out of an anchor bolt from concrete plate: Simulated crack patterns.

side of the anchor-head the crack grows tortuously in an almost horizontal direction towards the plate edge, which is similar to the observed crack pattern I presented in Fig. 25(a). Fig. 26(b) presents another crack pattern: on one side a diagonal crack propagates from the anchor head towards one of the fixing supports, and on the other side the crack propagates downward to the plate edge, resembling the observed crack pattern II shown in Fig. 25(b). The crack pattern depicted in Fig. 26(c) is nearly symmetric and the symmetry is broken once the crack branches on both sides as in Fig. 25(c).

Fig. 27(a) compares the load—displacement curves simulated by the MCS of 200 samples against the experimental results [70]. It is seen that the ascending regime and the peak load can be well captured by the probabilistic PF-CZM. Some discrepancies are observed in the post-peak behavior [73] due to the large scatters of loading processes reported in the test. The mean load—displacement curve is slightly lower than that the result of deterministic analysis. The numerically predicted CDF of the peak load is plot in Fig. 27(b). It is alarming to note that the peak load predicted by the deterministic analysis corresponds to a failure probability of 78%, which is unacceptably large for engineering design.

## 6. Conclusions

In this study, a computational framework by combining the random field and phase-field cohesive zone model is proposed for stochastic fracture in heterogeneous quasi-brittle solids. A cross-correlated bivariate random field

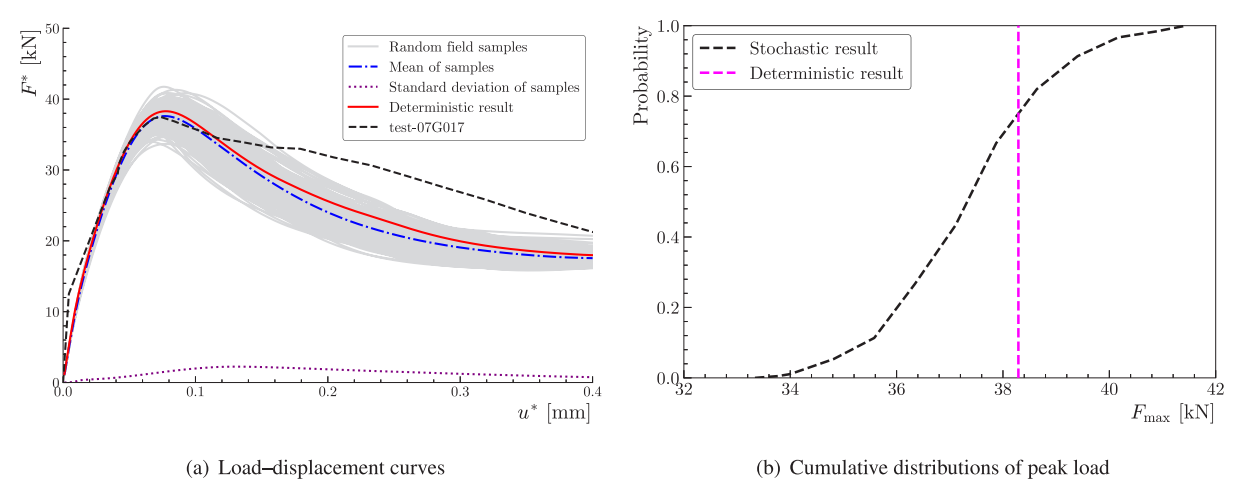


Fig. 27. Pull-out of an anchor bolt from concrete plate: Simulated load-displacement curves and cumulative distributions of peak load.

of lognormal distribution and the Karhunen–Loève expansion method are adopted to represent the spatial variation and the correlation between the failure strength and fracture energy. The phase-field cohesive zone model (PF-CZM) is then employed to deal with the resulting arbitrary crack nucleation and complicate propagation in heterogeneous quasi-brittle solids.

The model applies to the scenarios in which the fracture process zone (FPZ) width is significantly smaller than the correlation length of the random field of the material properties. In other words, the material properties inside the FPZ are locally homogeneous. In this case, the random field of the material properties can be locally projected to the finite element mesh and the objectivity of the stochastic numerical results is guaranteed. In the PF-CZM, this condition imposes an upper bound on the phase-field length scale parameter. The requirement can always be fulfilled since the phase-field length scale is a numerical parameter, which can be as small as possible.

The probabilistic PF-CZM is applied to the Monte-Carlo simulation of stochastic fracture in heterogeneous solids. Several representative numerical examples with non-uniform and uniform initial stress field are considered. It is confirmed that, upon the upper bound condition, the probabilistic PF-CZM is also insensitive to the phase-field length scale parameter and independent of the finite element mesh discretization, similarly to its deterministic counterpart. As the failure strength and fracture energy are intrinsically incorporated as two cross-correlated random material properties, the probabilistic PF-CZM is able to capture random crack nucleation, arbitrary crack propagation and multiple failure modes in heterogeneous quasi-brittle solids.

These numerical examples also indicate that the conventional deterministic analysis is often unable to predict and explain the experimentally observed complex crack patterns. Meanwhile, the deterministic analysis would also over-predict the mean load capacity. This finding highlights the important role of stochastic analysis in engineering designs.

## **Declaration of competing interest**

The authors declare that they have no known competing financial interests or personal relationships that could have appeared to influence the work reported in this paper.

## Data availability

Data will be made available on request.

## Acknowledgments

J. Y. Wu acknowledges the support from the National Natural Science Foundation of China (52125801; 51878294), State Key Laboratory of Disaster Reduction in Civil Engineering, China (SLDRCE20-01) and Guangdong Provincial Key Laboratory of Modern Civil Engineering Technology (2021B1212040003). J.-L. Le acknowledges the support from the U.S. National Science Foundation (Grant CMMI-2151209) to the University of Minnesota.

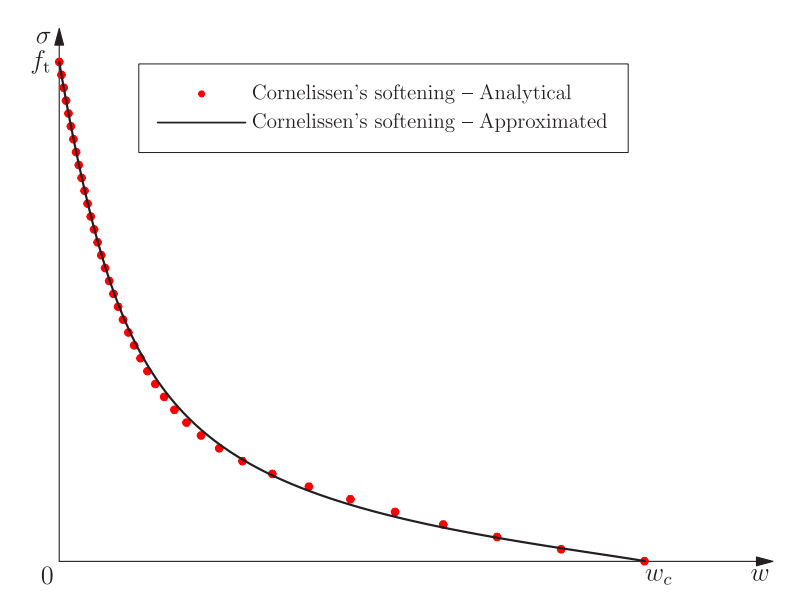


Fig. A.28. PF-CZM approximation of the Cornelissen et al. [37] softening law with the fourth-order polynomial P(d).

## Appendix. Approximation of the Cornelissen et al. [37] softening curve with higher polynomial P(d)

As stated in Remark 2.1, the PF-CZM approximation of the Cornelissen et al. [37] softening curve shown in Fig. 2(b) can be improved by introducing a higher-order polynomial or another type of function P(d). For instance, let us consider the following fourth-order polynomial

$$P(d) = 1 + a_2d + a_3d^2 + a_4d^3 + a_5d^4 + \cdots$$
(A.1)

where the parameter  $a_2$  is given from Eq.  $(2.4)_2$  as before, while the parameters  $a_3$ ,  $a_4$  and  $a_5$  satisfy the identity

$$a_3 + a_4 + a_5 + \dots = \frac{1}{2}\beta_w^2 - (1 + a_2)$$
 (A.2)

for the normalized ultimate crack opening  $\beta_w$  defined in Eq. (2.5)<sub>2</sub>. In order to determine the parameters  $a_3$ ,  $a_4$  and  $a_5$  uniquely, two extra characteristics of the softening curve  $\sigma(w)$ , e.g., the ultimate slope  $k_c$  at the failure crack opening  $w_c$ , the values ( $w_a$ ,  $\sigma_a$ ) at the articulate point, etc., can be considered. Alternately, they can be determined by the least-square fitting method or the simpler trial-error scheme. In Fig. A.28, the resulting PF-CZM approximation is shown for the following parameters

$$a_3 = 1.25, \qquad a_4 = 6.75, \qquad a_5 = -7.09$$
 (A.3)

As can be seen, the discrepancy from the Cornelissen et al. [37] softening curve is negligible and it will continue diminishing for higher-order polynomials.

#### References

- [1] E. Vanmarcke, Random Fields: Analysis and Synthesis, World scientific, 2010.
- [2] Y. Huang, Z. Yang, X. Chen, G. Liu, Monte Carlo simulations of meso-scale dynamic compressive behavior of concrete based on X-ray computed tomography images, Int. J. Impact Eng. 97 (2016) 102–115.
- [3] Z. Yang, W. Ren, R. Sharma, S. McDonald, M. Mostafavi, Y. Vertyagina, T. Marrow, In-situ X-ray computed tomography characterisation of 3D fracture evolution and image-based numerical homogenisation of concrete, Cem. Concr. Compos. 75 (2017) 74–83.
- [4] N.R. Ravahatra, F. Duprat, F. Schoefs, T. de Larrard, E. Bastidas-Arteaga, Assessing the capability of analytical carbonation models to propagate uncertainties and spatial variability of reinforced concrete structures, Front. Built Environ. 3 (2017) 1.
- [5] T. Xu, J. Li, Assessing the spatial variability of the concrete by the rebound hammer test and compression test of drilled cores, Constr. Build. Mater. 188 (2018) 820–832.

- [6] D. Breysse, Nondestructive evaluation of concrete strength: An historical review and a new perspective by combining NDT methods, Constr. Build. Mater. 33 (2012) 139–163.
- [7] N.T. Nguyen, Z.-M. Sbartaï, J.-F. Lataste, D. Breysse, F. Bos, Assessing the spatial variability of concrete structures using NDT techniques—Laboratory tests and case study, Constr. Build. Mater. 49 (2013) 240–250.
- [8] Z. Yang, X. Su, J.F. Chen, G. Liu, Monte Carlo simulation of complex cohesive fracture in random heterogeneous quasi-brittle materials, Int. J. Solids Struct. 46 (17) (2009) 3222–3234.
- [9] P.L. Clarke, R. Abedi, B. Bahmani, K.A. Acton, S.C. Baxter, Effect of the spatial inhomogeneity of fracture strength on fracture pattern for quasi-brittle materials, in: ASME International Mechanical Engineering Congress and Exposition, Vol. 58448, American Society of Mechanical Engineers, 2017, V009T12A045.
- [10] J. Li, L. Hai, T. Xu, Two-scale random field model for quasi-brittle materials, Probab. Eng. Mech. 66 (2021) 103154.
- [11] T. Rabczuk, Computational methods for fracture in brittle and quasi-brittle solids: State-of-the-art review and future perspectives, ISRN Appl. Math. 2013 (2013) http://dx.doi.org/10.1155/2013/849231.
- [12] T. Most, C. Bucher, Stochastic simulation of cracking in concrete structures using multiparameter random fields, Int. J. Reliab. Saf. 1 (1–2) (2006) 168–187.
- [13] Z. Yang, X.F. Xu, A heterogeneous cohesive model for quasi-brittle materials considering spatially varying random fracture properties, Comput. Methods Appl. Mech. Engrg. 197 (45–48) (2008) 4027–4039.
- [14] Z.P. Bažant, J.-L. Le, M. Salviato, Quasibrittle Fracture Mechanics: A First Course, Oxford University Press, Oxford, U.K., 2021.
- [15] J. Carmeliet, H. Hens, Probabilistic nonlocal damage model for continua with random field properties, J. Eng. Mech. 120 (10) (1994) 2013–2027.
- [16] D. Castillo, T.H. Nguyen, J. Niiranen, Spatially random modulus and tensile strength: Contribution to variability of strain, damage, and fracture in concrete, Int. J. Damage Mech. (2021) 10567895211013081.
- [17] A. Krayani, G. Pijaudier-Cabot, F. Dufour, Boundary effect on weight function in nonlocal damage model, Engineering Fracture Mechanics 76 (14) (2009) 2217–2231.
- [18] Z.P. Bažant, J.-L. Le, C.G. Hoover, Nonlocal boundary layer model: Overcoming boundary condition problems in strength statistics and fracture analysis of quasibrittle materials, in: Fracture Mechanics of Concrete and Concrete Structures—Recent Advances in Fracture Mechanics of Concrete, Jeju, Korea, 2010, pp. 135–143.
- [19] Z. Bažant, J.-L. Le, Probabilistic Mechanics of Quasibrittle Structures: Strength, Lifetime, and Size Effect, Cambridge University Press, Cambridge, U.K., 2017.
- [20] J.-L. Le, J. Eliáš, A probabilistic crack band model for quasibrittle fracture, J. Appl. Mech. 83 (5) (2016).
- [21] A. Gorgogianni, J. Eliáš, J.-L. Le, Mesh objective stochastic simulations of quasibrittle fracture, J. Mech. Phys. Solids 159 (2022) 104745
- [22] G.A. Francfort, J.-J. Marigo, Revisiting brittle fracture as an energy minimization problem, J. Mech. Phys. Solids 46 (8) (1998) 1319–1342.
- [23] B. Bourdin, G.A. Francfort, J.-J. Marigo, Numerical experiments in revisited brittle fracture, J. Mech. Phys. Solids 48 (4) (2000)
- [24] B. Bourdin, G.A. Francfort, J.-J. Marigo, The variational approach to fracture, J. Elasticity 91 (1-3) (2008) 5-148.
- [25] K. Pham, H. Amor, J.-J. Marigo, C. Maurini, Gradient damage models and their use to approximate brittle fracture, Int. J. Damage Mech. 20 (4) (2011) 618–652.
- [26] C. Kuhn, A. Schlüter, R. Müller, On degradation functions in phase field fracture models, Comput. Mater. Sci. 108 (2015) 374–384.
- [27] C. Miehe, M. Hofacker, F. Welschinger, A phase field model for rate-independent crack propagation: Robust algorithmic implementation based on operator splits, Comput. Methods Appl. Mech. Engrg. 199 (45–48) (2010) 2765–2778.
- [28] E. Gironacci, M.M. Nezhad, M. Rezania, G. Lancioni, A non-local probabilistic method for modeling of crack propagation, Int. J. Mech. Sci. 144 (2018) 897–908.
- [29] D.-A. Hun, J. Guilleminot, J. Yvonnet, M. Bornert, Stochastic multiscale modeling of crack propagation in random heterogeneous media, Internat. J. Numer. Methods Engrg. 119 (13) (2019) 1325–1344.
- [30] B. Gajdics, J.J. Tomán, H. Zapolsky, Z. Erdélyi, G. Demange, A multiscale procedure based on the stochastic kinetic mean field and the phase-field models for coarsening, J. Appl. Phys. 126 (6) (2019) 065106.
- [31] N. Nguyen, J. Yvonnet, J. Réthoré, A.B. Tran, Identification of fracture models based on phase field for crack propagation in heterogeneous lattices in a context of non-separated scales, Comput. Mech. 63 (5) (2019) 1047–1068.
- [32] T. Gerasimov, U. Römer, J. Vondřejc, H.G. Matthies, L. De Lorenzis, Stochastic phase-field modeling of brittle fracture: Computing multiple crack patterns and their probabilities, Comput. Methods Appl. Mech. Engrg. 372 (2020) 113353.
- [33] J.-Y. Wu, A unified phase-field theory for the mechanics of damage and quasi-brittle failure, J. Mech. Phys. Solids 103 (2017) 72-99.
- [34] J.-Y. Wu, A geometrically regularized gradient-damage model with energetic equivalence, Comput. Methods Appl. Mech. Engrg. 328 (2018) 612–637.
- [35] J.-Y. Wu, V.P. Nguyen, A length scale insensitive phase-field damage model for brittle fracture, J. Mech. Phys. Solids 119 (2018) 20–42.
- [36] T.K. Mandal, V.P. Nguyen, J.-Y. Wu, Length scale and mesh bias sensitivity of phase-field models for brittle and cohesive fracture, Eng. Fract. Mech. 217 (2019) 106532.
- [37] H. Cornelissen, D. Hordijk, H. Reinhardt, Experimental determination of crack softening characteristics of normalweight and lightweight, Heron 31 (2) (1986) 45–46.
- [38] Z.-J. Yang, B.-B. Li, J.-Y. Wu, X-ray computed tomography images based phase-field modeling of mesoscopic failure in concrete, Eng. Fract. Mech. 208 (2019) 151–170.

- [39] Y. Huang, H. Zhang, B. Li, Z. Yang, J. Wu, P. Withers, Generation of high-fidelity random fields from micro CT images and phase field-based mesoscale fracture modelling of concrete, Eng. Fract. Mech. 249 (2021) 107762.
- [40] L. Hai, J. Li, Modeling tensile damage and fracture of quasi-brittle materials using stochastic phase-field model, Theor. Appl. Fract. Mech. 118 (2022) 103283.
- [41] Z.P. Bažant, B.H. Oh, Crack band theory for fracture of concrete, Matér. Constr. 16 (3) (1983) 155-177.
- [42] L. Hai, Phase-Field Theory for Fracture and Multi-Scale Damage Model of Concrete (Ph.D. thesis), Tongji University, 2022.
- [43] C. Miehe, F. Welschinger, M. Hofacker, Thermodynamically consistent phase-field models of fracture: Variational principles and multi-field FE implementations, Internat. J. Numer. Methods Engrg. 83 (10) (2010) 1273–1311.
- [44] J.-Y. Wu, V.P. Nguyen, H. Zhou, Y. Huang, A variationally consistent phase-field anisotropic damage model for fracture, Comput. Methods Appl. Mech. Engrg. 358 (2020) 112629.
- [45] Y. Feng, J. Fan, J. Li, Endowing explicit cohesive laws to the phase-field fracture theory, J. Mech. Phys. Solids 152 (2021) 104464.
- [46] D. Feng, J. Wu, Phase-field regularized cohesive zone model (CZM) and size effect of concrete, Eng. Fract. Mech. 197 (2018) 66-79.
- [47] J. Eliáš, M. Vořechovský, J. Skoček, Z.P. Bažant, Stochastic discrete meso-scale simulations of concrete fracture: Comparison to experimental data, Eng. Fract. Mech. 135 (2015) 1–16.
- [48] Z.P. Bažant, J.-L. Le, M.Z. Bazant, Scaling of strength and lifetime distributions of quasibrittle structures based on atomistic fracture mechanics, 106 (2009) 11484–11489.
- [49] J.-L. Le, Z.P. Bažant, M.Z. Bažant, Unified nano-mechanics based probabilistic theory of quasibrittle and brittle structures: I. Strength, static crack growth, lifetime and scaling, J. Mech. Phys. Solids 59 (7) (2011) 1291–1321.
- [50] P.-L. Liu, A. Der Kiureghian, Multivariate distribution models with prescribed marginals and covariances, Probab. Eng. Mech. 1 (2) (1986) 105–112.
- [51] H. Li, Z. Lü, X. Yuan, Nataf transformation based point estimate method, Chin. Sci. Bull. 53 (17) (2008) 2586-2592.
- [52] P.D. Spanos, R. Ghanem, Stochastic finite element expansion for random media, J. Eng. Mech. 115 (5) (1989) 1035-1053.
- [53] K. Phoon, S. Huang, S. Quek, Implementation of Karhunen-Loeve expansion for simulation using a wavelet-Galerkin scheme, Probab. Eng. Mech. 17 (3) (2002) 293–303.
- [54] R.G. Ghanem, P.D. Spanos, Stochastic Finite Elements: A Spectral Approach, Courier Corporation, 2003.
- [55] L. Wang, Karhunen-Loeve Expansions and their Applications, London School of Economics and Political Science, United Kingdom, 2008.
- [56] M. Vořechovský, Simulation of simply cross correlated random fields by series expansion methods, Struct. Saf. 30 (4) (2008) 337–363.
- [57] Z.P. Bažant, G. Pijaudier-Cabot, Measurement of characteristic length of nonlocal continuum, J. Eng. Mech. ASCE 115 (4) (1989) 755–767.
- [58] A. Der Kiureghian, J.-B. Ke, The stochastic finite element method in structural reliability, Probab. Eng. Mech. 3 (2) (1988) 83-91.
- [59] K.A. Vu, M.G. Stewart, Predicting the likelihood and extent of reinforced concrete corrosion-induced cracking, J. Struct. Eng. 131 (11) (2005) 1681–1689.
- [60] M. Mousavi Nezhad, E. Gironacci, M. Rezania, N. Khalili, Stochastic modelling of crack propagation in materials with random properties using isometric mapping for dimensionality reduction of nonlinear data sets, Internat. J. Numer. Methods Engrg. 113 (4) (2018) 656–680.
- [61] J.-Y. Wu, Y. Huang, V.P. Nguyen, On the BFGS monolithic algorithm for the unified phase field damage theory, Comput. Methods Appl. Mech. Engrg. 360 (2020) 112704.
- [62] J.-Y. Wu, Y. Huang, Comprehensive implementations of phase-field damage models in Abaqus, Theor. Appl. Fract. Mech. 106 (2020) 102440.
- [63] J.-Y. Wu, Y. Huang, H. Zhou, V.P. Nguyen, Three-dimensional phase-field modeling of mode I+ II/III failure in solids, Comput. Methods Appl. Mech. Engrg. 373 (2021) 113537.
- [64] P.K. Kristensen, E. Martínez-Pañeda, Phase field fracture modelling using quasi-Newton methods and a new adaptive step scheme, Theor. Appl. Fract. Mech. 107 (2020) 102446.
- [65] T.K. Mandal, V.P. Nguyen, J.-Y. Wu, C. Nguyen-Thanh, A. de Vaucorbeil, Fracture of thermo-elastic solids: Phase-field modeling and new results with an efficient monolithic solver, Comput. Methods Appl. Mech. Engrg. 376 (2021) 113648.
- [66] H. Amor, J. Marigo, C. Maurini, Regularized formulation of the variational brittle fracture with unilateral contact: Numerical experiments, J. Mech. Phys. Solids 57 (2009) 1209–1229.
- [67] Z. Xu, J.-L. Le, A first passage model for probabilistic failure of polycrystalline silicon MEMS structures, J. Mech. Phys. Solids 99 (2017) 225–241.
- [68] J.-L. Le, Level excursion analysis of probabilistic quasibrittle fracture, Sci. China: Technol. Sci. 63 (7) (2020) 1141–1153.
- [69] C.G. Hoover, Z.P. Bažant, J. Vorel, R. Wendner, M.H. Hubler, Comprehensive concrete fracture tests: Description and results, Eng. Fract. Mech. 114 (2013) 92–103.
- [70] A. Vervuurt, J.G. Van Mier, E. Schlangen, Analyses of anchor pull-out in concrete, Mater. Struct. 27 (5) (1994) 251–259.
- [71] A. Vervuurt, J.G. Van Mier, E. Schlangen, Experiments of steel anchors embedded in concrete, in: L. Elfgren (Ed.), RILEM Technical Committee 90-FMA, Technical Report. Rots, Research Report 1998: 14, Division of Structural Engineering, Lulea University of Technology, Sweden, 1998.
- [72] R.d. de Borst, Some recent issues in computational failure mechanics, Internat. J. Numer. Methods Engrg. 52 (1-2) (2001) 63-95.
- [73] P. Soparat, P. Nanakorn, Analysis of anchor bolt pullout in concrete by the element-free Galerkin method, Eng. Struct. 30 (12) (2008) 3574–3586.
- [74] M. Gutiérrez, R. De Borst, Deterministic and stochastic analysis of size effects and damage evolution in quasi-brittle materials, Arch. Appl. Mech. 69 (9) (1999) 655–676.

- [75] C. Xu, C. Heping, L. Bin, Z. Fangfang, Modeling of anchor bolt pullout in concrete based on a heterogeneous assumption, Nucl. Eng. Des. 241 (5) (2011) 1345–1351.
- [76] P. Wu, J. Zhao, Z. Chen, F. Bobaru, Validation of a stochastically homogenized peridynamic model for quasi-static fracture in concrete, Eng. Fract. Mech. 237 (2020) 107293.